

UKAEA-CCFE-PR(23)181

P. A. Schneider, C. Angioni, F. Auriemma, N.  
Bonanomi, T. Görler, R. Henriques, L. Horvath, D.  
King, H. Nyström, M. Maslov, J. Ruiz, G. Szepesi, C.  
Challis, E. Delabie, J. M. Fontdecaba, L. Frassinetti,  
G. Garcia, C. Giroud, J. Hillesheim, J. Hobirk, A.

Kappatou, D. L. Keeling, M. Lennholm, B.  
Lomanowski, T. Luda di Cortenaglia, R. Lorenzini, C.  
F. Maggi, S. Menemir, A. Thoman

**isotope physics of heat and particle  
transport with tritium in JET-ILW H-  
mode plasmas**

Enquiries about copyright and reproduction should in the first instance be addressed to the UKAEA Publications Officer, Culham Science Centre, Building K1/O/83 Abingdon, Oxfordshire, OX14 3DB, UK. The United Kingdom Atomic Energy Authority is the copyright holder.

The contents of this document and all other UKAEA Preprints, Reports and Conference Papers are available to view online free at [scientific-publications.ukaea.uk/](https://scientific-publications.ukaea.uk/)

# isotope physics of heat and particle transport with tritium in JET-ILW H-mode plasmas

P. A. Schneider, C. Angioni, F. Auriemma, N. Bonanomi, T. Görler, R. Henriques, L. Horvath, D. King, H. Nyström, M. Maslov, J. Ruiz, G. Szepesi, C. Challis, E. Delabie, J. M. Fontdecaba, L. Frassinetti, G. Garcia, C. Giroud, J. Hillesheim, J. Hobirk, A. Kappatou, D. L. Keeling, M. Lennholm, B. Lomanowski, T. Luda di Cortemiglia, R. Lorenzini, C. F. Maggi, S. Menmuir, A. Thorman



# Isotope physics of heat and particle transport with tritium in JET-ILW type-I ELMy H-mode plasmas

P. A. Schneider<sup>1</sup>, C. Angioni<sup>1</sup>, F. Auriemma<sup>2</sup>, N. Bonanomi<sup>1</sup>, T. Görler<sup>1</sup>, R. Henriques<sup>3</sup>, L. Horvath<sup>4, 5</sup>, D. King<sup>4</sup>, R. Lorenzini<sup>2</sup>, H. Nyström<sup>6</sup>, M. Maslov<sup>4</sup>, J. Ruiz<sup>7</sup>, G. Szepesi<sup>4</sup>, C. D. Challis<sup>4</sup>, A. Chomiczewska<sup>8</sup>, E. Delabie<sup>9</sup>, J. M. Fontdecaba<sup>10</sup>, L. Frassinetti<sup>6</sup>, J. Garcia<sup>11</sup>, C. Giroud<sup>4</sup>, J. Hillesheim<sup>4</sup>, J. Hobirk<sup>1</sup>, A. Kappatou<sup>1</sup>, D. L. Keeling<sup>4</sup>, E. Kowalska-Strzeciwilk<sup>8</sup>, M. Lennholm<sup>4</sup>, B. Lomanowski<sup>9</sup>, T. Luda di Cortemiglia<sup>1</sup>, C. F. Maggi<sup>4</sup>, S. Menmuir<sup>4</sup>, G. Pucella<sup>12</sup>, A. Thorman<sup>4</sup> and JET Contributors\*

<sup>1</sup>Max-Planck-Institut für Plasmaphysik, Boltzmannstr. 2, 85748 Garching, Germany

<sup>2</sup>Consorzio RFX-CNR, ENEA, INFN, Università di Padova, Acciaierie Venete SpA, Padova, Italy, CNR-ISTP, Corso Stati Uniti 4, 35127 Padova, Italy

<sup>3</sup>Instituto de Plasmas e Fusão Nuclear, Instituto Superior Técnico, Universidade de Lisboa, Lisboa, Portugal

<sup>4</sup>United Kingdom Atomic Energy Authority, Culham Science Centre, Abingdon, Oxon, OX14 3DB, UK

<sup>5</sup>Princeton Plasma Physics Laboratory, Princeton, New Jersey 08540, USA

<sup>6</sup>KTH Royal Institute of Technology, Teknikringen 31, Sweden

<sup>7</sup>Rudolf Peierls Centre for Theoretical Physics, University of Oxford, Oxford OX1 3PU, United Kingdom

<sup>8</sup>Institute of Plasma Physics and Laser Microfusion, Warsaw, Poland

<sup>9</sup>Oak Ridge National Laboratory, Oak Ridge, Tennessee, United States of America

<sup>10</sup>Laboratorio Nacional de Fusión Ciemat, E-28040 Madrid, Spain

<sup>11</sup>CEA, IRFM, F-13108 Saint-Paul-lez-Durance, France

<sup>12</sup>Dip.to Fusione e Tecnologie per la Sicurezza Nucleare, ENEA C. R. Frascati, via E. Fermi 45, 00044 Frascati (Roma), Italy

\*See author list of J. Mailloux et al 2022 Nucl. Fusion 62 042026

## Abstract:

During the DTE2 campaign in the JET tokamak we performed a parameter scan in T and D-T complementing existing pulses in H and D. For the different main ion masses type-I ELMy H-modes at fixed plasma current and magnetic field can have the pedestal pressure varying by a factor of 4 and the total pressure changing from  $\beta_N = 1.0$  to 3.0. Based on this wide data set the pedestal and core isotope mass dependencies are investigated. The pedestal shows a strong mass dependence in the density which influences the core due to the strong coupling between both plasma regions.

To understand the key causes for the observed isotope mass dependence in the pedestal it is important to unscramble the interplay between heat and particle transport and the ELM stability. For this purpose we developed a dynamic ELM cycle model with basic transport assumptions and a realistic neutral penetration. This model highlights that a mass dependence in the ELM stability or in the transport alone cannot explain the observations. One requires a mass dependence in the ELM stability as well as one in the particle transport. Additionally, heat and particle transport require different mass dependencies.

The core confinement time increases with pedestal pressure for all isotope masses due to profile stiffness and electromagnetic turbulence stabilisation. Additional to the general trend we observe T and D-T plasmas with an improved core confinement time compared to H and D plasmas even for matched pedestal pressures. For T a large part of this improvement can be attributed to the unique pedestal composition of higher densities and lower temperatures than H and D. With a reduced gyroBohm factor at lower temperatures more turbulent drive in the form of steeper gradients is required to transport the same amount of heat. This picture is supported by quasilinear flux driven modelling using TGLF-SAT2 within ASTRA. With the experimental boundary condition TGLF-SAT2 predicts the core profiles well for gyroBohm heat fluxes  $> 15$ , however, overestimates the heat and particle transport closer to the turbulent threshold.

## 1 Introduction

For densities and temperatures typical for magnetically confined plasmas the most favorable fusion cross sections are those of reactions between the hydrogen isotopes deuterium (D)

and tritium (T). Therefore, since the beginning of research with magnetically confinement devices like tokamaks one question was always investigated: How does the mass number of the main ions  $A$  impact the physics of the plasma? Since answering this question is a fundamental requirement to transfer knowledge gained in experiments and modelling with the lighter isotopes H and D towards D-T fusion plasmas. Early on it was quite clear that the multitude of different observations [1] cannot be explained with just a single physics concept, but they require the interplay of multiple mechanisms. One crucial challenge with investigating isotope mass related physics is that in experiment it is extremely difficult to vary just the isotope mass. The inevitable differences occurring in experiments might be dominating the results, which makes it difficult to quantify the subdominant mass dependence. Additionally, the relevance of these changes can vary depending on plasma regime.

In electron heated L-mode and Ohmic plasmas it was found that the mass dependence of the electron-ion equipartition can cause a change in confinement time [2–4], just changing the heating mix or mitigating the importance of the equipartition by reducing the density will change this mass dependence. When the equipartition does not play a role the core transport can be found without mass dependence [5].

In H-mode plasmas the coupling between core and edge is essential to understand the observed plasma states [6]. We know that the H-mode pedestal shows a strong isotope mass dependence where plasmas with heavier ions have higher pedestal top pressures [7–15]. Consequently, an experimental investigation of the core transport ideally starts with matched pedestal conditions. However, to achieve this we need to offset the pedestal mass dependence. Varying the heating power is one option [9, 10], however, then profile stiffness [16] and the associated power degradation will play an important role causing the relative relevance of  $A$  to decrease and the uncertainties in the measured mass dependence to increase. Adjusting the gas fuelling to offset the edge mass dependence will also influence the global confinement [6, 10, 13]. A third method which has been employed is adjusting the plasma triangularity [13, 15]. While the plasma shape can also influence the core heat transport [17] it appears to be the least invasive of the three methods, since its impact on the pedestal is more pronounced than the potential influence in the core.

With matched edge conditions we can find experimental regimes with a very weak mass dependence in the core [7, 8, 15] and those with a strong mass dependence [13, 18, 19]. In the more recent studies with a strong mass dependence in AUG and JET-ILW plasmas [13, 19] this could be attributed to a higher fast-ion content in plasmas with heavier main ions. These differences arise due to different heating methods and the mass dependence in the fast-ion slowing down. This fast-ion turbulence stabilisation is also a potential explanation why D-T supershots in TFTR exhibited a stronger mass dependence in the core than pulses with less heating power [18].

The story of the mass dependence in theory is not less diverse than the experimental observations. Depending on the dominant turbulence type the mass dependence is expected to be different. In general, theoretical mass dependencies are quantified relative to the micro-turbulence or gyroBohm scaling [20] with the gyroBohm diffusivity  $\chi_{gB} \propto T^{\frac{3}{2}} A^{\frac{1}{2}} / (RB^2)$  or the gyroBohm heat flux  $q_{gB} \propto T^{\frac{5}{2}} A^{\frac{1}{2}} n / (R^2 B^2)$  where  $T$  is the plasma temperature,  $n$  the plasma density,  $R$  the major radius and  $B$  the magnetic field. Since this increased transport with higher isotope mass is not observed experimentally, theory often tries to explain which physics mechanisms can cause a gyroBohm breaking or anti-gyroBohm scaling - i.e. having a heat transport which reduces with increasing mass.

For the ion temperature gradient driven turbulence ITG, which is also dominant in the core of the plasmas discussed here, we expect a gyroBohm mass scaling only in the collisionless limit [13, 21]. Collisions, electromagnetic EM effects and  $E \times B$  shearing  $\gamma_{E \times B}$  can introduce mass dependencies [22] which can ultimately cause a gyroBohm breaking [21]. Since the importance of these mechanisms can greatly vary for different experimental conditions - i.e. flat rotation profile vs. peaked rotation profile - so does the expected mass dependence. For trapped electron mode turbulence TEM a weakening of the gyroBohm mass dependence can be caused by zonal flow regulation of the turbulence when  $T_e \sim T_i$ , for  $T_e \gg T_i$  the mass scaling is again gyroBohm like [23].

In the plasma edge of L-modes, where the density gradients are steeper than in the core, collisional drift waves can become dominant and the finite electron-to-ion mass-ratio dependence

of the nonadiabatic electron response introduces an anti-gyroBohm like mass dependence of the transport [24, 25]. In the H-mode pedestal also the temperature gradients increase and electron temperature gradient ETG driven turbulence can contribute significantly to the electron heat flux while showing no mass dependence [26]. However, for these H-mode pedestal parameters the ITG turbulence drives strong anti-gyroBohm heat fluxes due to differences of  $\gamma_{E \times B}$  when varying the mass. In the steep gradient region the neoclassical transport also contributes to the heat and particle transport and has a more gyroBohm like mass dependence, such that in the total heat transport the opposite mass dependencies cancel out [26]. The total particle transport retains the mass dependence of the ITG turbulence since the neoclassical particle transport is mostly mass independent [26].

The unifying feature of all those theoretical studies is that no universal mass scaling of the transport is expected, but the mass dependence will change with the actual plasma regime that is considered. This is consistent with the variety of experimental observations and highlights the importance to perform experiments using pure T and D-T mixtures and not entirely rely on extrapolations from H and D plasmas. To quantify the impact of the isotope mass on heat and particle transport it is important to minimize secondary effects due to experimental differences and take the differences into account in the interpretation where they are unavoidable. The dynamic nature of the H-mode pedestal with edge localized modes ELMs and the coupling of the core and edge transport regions and coupling of electron and ion transport channels are prime examples of interactions which need to be taken into account. This results in a complex system of often non-linear interactions which need to be modelled. The high fidelity theoretical models discussed above are not suited for this purpose, where full radius flux driven modelling is required. Instead we rely on the quasilinear TGLF-SAT2 [27] model which does not simulate the full non-linear physics but utilizes linear growth rates and estimates heat and particle fluxes based on a saturation rule - here SAT2. SAT2 is optimised based on the solutions of non-linear CGYRO [28] simulations over a wide range of parameters. However, it was calibrated on deuterium plasmas. While this reduced model is not expected to capture the full physics it should reproduce the leading contributions to heat and particle transport. Recently, an extension to the saturation rule 2 has been proposed in the form of SAT3 [29] which captures the gyroBohm breaking CGYRO predicts for high density gradients  $a/L_{ne} > 2.0$  [25].  $a/L_{ne} > 2.0$  corresponds to the steep gradient region in the pedestal which is in contrast to the core region with  $a/L_{ne} < 1.0$ . In the core also Sat2 captures the mass dependence suggested by CGYRO which is a bit stronger than gyroBohm like [29].

State of the art would be to use integrated models which couple scrape off layer, pedestal and core [30]. However, these lack flexibility in testing the individual mass dependencies and we know that parts of the models do not capture isotope physics well. In particular, the pedestal part of the model which relies on ideal peeling-ballooning stability does not reproduce the observed isotope mass dependencies [14]. Therefore, we investigate the pedestal and core separately while also quantifying the coupling between both.

In section 2 we will describe how the experiments are performed in the JET tokamak and discuss basic engineering constraints that arise when operating with different isotopes. Section 3 introduces and describes the analysis procedures used to obtain the presented data. In section 4 first we introduce and apply a dynamic ELM cycle model to understand the relative importance of transport processes and stability limits in the pedestal. Then we utilize the TGLF-SAT2 transport code to investigate core-edge coupling based of transport properties. Section 5 gives an overview of the experimental observations in the pedestal region and section 6 describes the ideal peeling-ballooning stability analysis of the pedestal. The results of the experimental observations and the modelling are then discussed in section 7. The following sections on the plasma core have a similar structure, first we describe the observations in section 8, then report in section 9 on modelling with the quasilinear TGLF-SAT2 model and show linear as well non-linear gyrokinetic GENE simulations. The implications of experimental observations and core modelling results are discussed in section 10. The key results of this paper are then summarized in section 11.

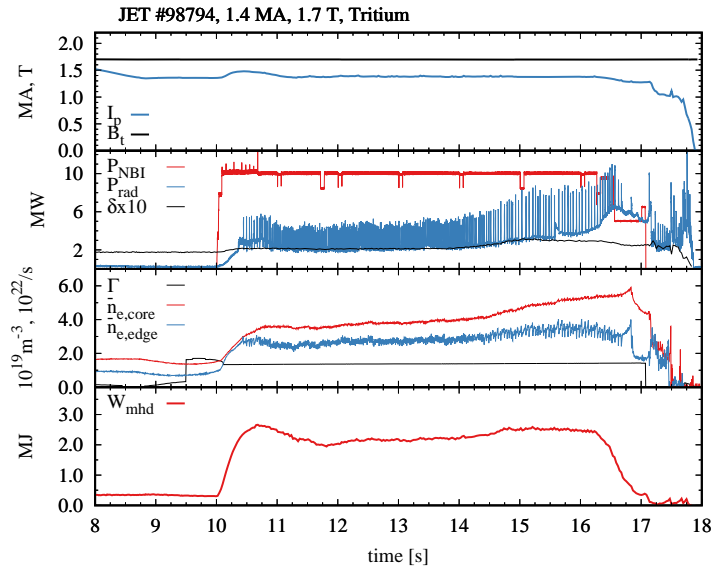


FIG. 1: Timetraces for a typical plasma pulse in T, from top to bottom plasma current  $I_p$  and magnetic field  $B_t$ , auxiliary heating power  $P_{NBI}$  and radiated power  $P_{rad}$  and average triangularity  $\delta$ , core and edge line averaged densities  $\bar{n}_e$  and the gas flow rate  $\Gamma$ , total plasma stored energy  $W_{MHD}$ .

## 2 Experimental setup

The scenario used for this experimental study is a type-I ELMy H-mode with a plasma current of  $I_p = 1.4$  MA, a magnetic field of  $B_t = 1.7$  T, an edge safety factor of  $q_{95} = 3.7$  and the corner-corner CC divertor configuration. This type of plasma has been extensively studied at JET [6,11,15,31–34] and its properties in hydrogen and deuterium are well known. The main reasons for choosing this type of plasma is the relatively low heating power 12–15 MW required to reach high plasma pressure, this allows for a reasonable flexibility and it is possible to scan the normalised total plasma pressure  $\beta_N$  from 1.0 up to 3.0. In the CC divertor configuration, with the inner and outer strike points positioned in their respective divertor corners close to the pumping ducts, low densities are accessible which are required to reach high  $\beta_N$ . Additionally, the CC configuration is commonly used for most experiments and consequently those divertor tiles are relatively clean which is beneficial for the reproducibility of experiments. Experiments which utilize more uncommon divertor configurations often need to spend time on conditioning the divertor tiles first to ensure reproducible conditions.

**Pulse setup:** A typical setup for a plasma pulse is illustrated in figure 1. In the current flattop phase constant heating power is applied along with a constant gas fuelling. The flattop is divided in a low triangularity  $\delta$  phase up to 14.0 s and a high  $\delta$  phase starting at 15.0 s. Highly shaped plasmas or those with high  $\beta_N$  tend to not reach the planned termination due to impurity accumulation. The profile and transport analysis is then performed for the longest stationary phase before the onset of impurity accumulation. These phases typically have a length of  $> 10\tau_E$  where  $\tau_E$  is the energy confinement time, however, at  $\beta_N = 3.0$  the length goes down to  $2\tau_E$ .

**Heating:** The auxiliary heating power by neutral beam injection (NBI)  $P_{NBI}$  for our data set is varied from 3 up to 15 MW with the bulk of the experiments performed at 10 MW which results in a type-I ELMy H-mode for all main ion masses. The NBI species is D for most H and all D plasmas and T for the T plasmas. In DT both D- and T-NBI are utilized. The power calibration for D and T NBI is accurate within 10% [35]. Due to the low plasma density the NBI needs to be operated at reduced voltage  $\leq 100$  kV and reduced power per injector to avoid excessive NBI shinethrough. Along with the less than 100% availability of the neutral beams this prevented a sophisticated optimisation of the heating profiles for the different NBI and main ion species. The power density to electron and ions due to NBI as calculated with the NUBEAM [36] package within the TRANSP [37] code is illustrated for the different isotopes with varying density and  $P_{NBI} = 10$  MW in figure 2. Despite the lack of dedicated optimisation the heat profiles are well matched for  $\rho_{tor} > 0.3$  for all three isotopes and for H and T over the whole radius (for the definition of the radial coordinate

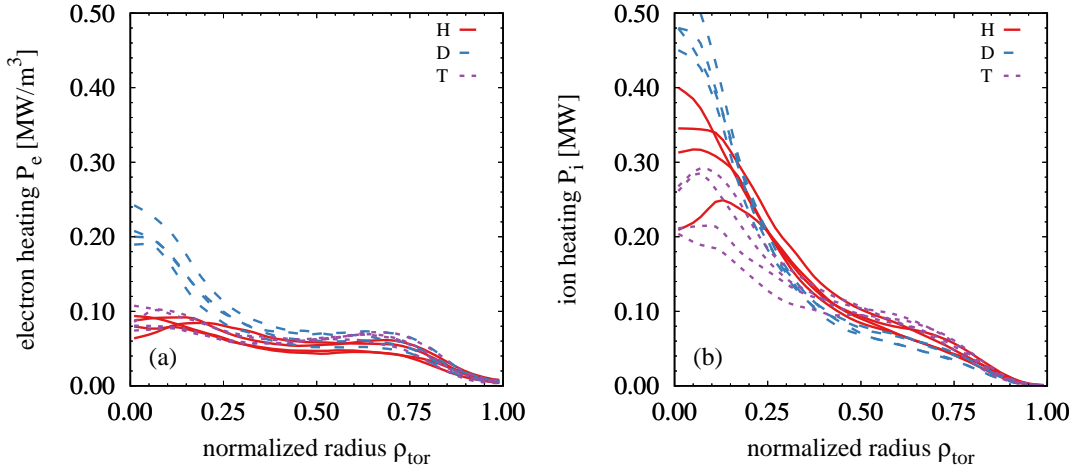


FIG. 2: Electron and ion heating for  $P_{\text{NBI}} = 10$  MW for different isotopes and densities.

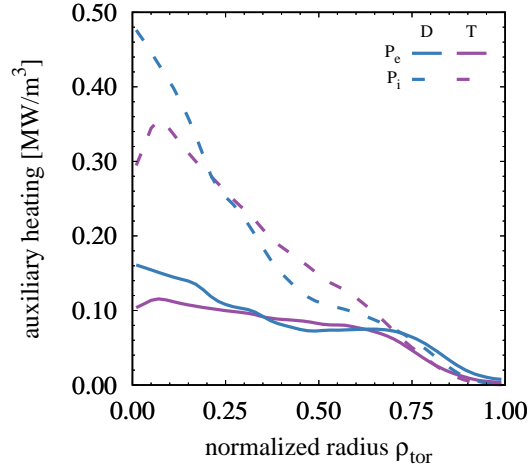


FIG. 3: Electron and ion heating for  $P_{\text{NBI}} = 13$  MW for T-NBI into T (JPN99224) and D-NBI into D (JPN97512) at similar densities.

see section 3). The D pulses tend to have more peaked heating profiles in the very center. However, due to the smaller volume for  $\rho_{\text{tor}} < 0.3$  the central heating amounts only to 30% of the total heating despite having more than 5 times the power density than at the outer radii. The differences in the heating profiles are taken into account in the modelling.

At the higher heating powers 13 MW, which are required to reach high  $\beta_{\text{N}}$ , the heat deposition is fairly similar due to overall higher plasma density. This is illustrated for D and T plasmas in a matched density case in figure 3. Note the higher ion heating due to the NBI in all cases. In the DT plasmas also  $\alpha$  heating due to D-T fusion reactions might play a role, however, for the parameters discussed here this is estimated to be only around 0.15 MW which is below 2% of the total heating power and will be neglected in the analysis. The fast-ion pressure calculated by TRANSP for the density matched plasmas in D and T is shown in figure 4, while the relative fast-ion energy is quite similar with  $W_{\text{fast}}/W_{\text{th}}|_{\text{D}} = 0.22$  and  $W_{\text{fast}}/W_{\text{th}}|_{\text{T}} = 0.24$ , there are differences in the fast-ion pressure gradients at the outer radii.

**Gas fuelling:** The gas fuelling during the current flattop phase is done with divertor valves. For the gases hydrogen, deuterium and neon the standard gas introductory modules GIMs can be used, for tritium only the tritium introductory modules TIMs are available [38]. This introduces an operational difference regarding fuelling with T compared to other gases. The TIMs are farther away from the main plasma chamber, therefore, there is a considerable

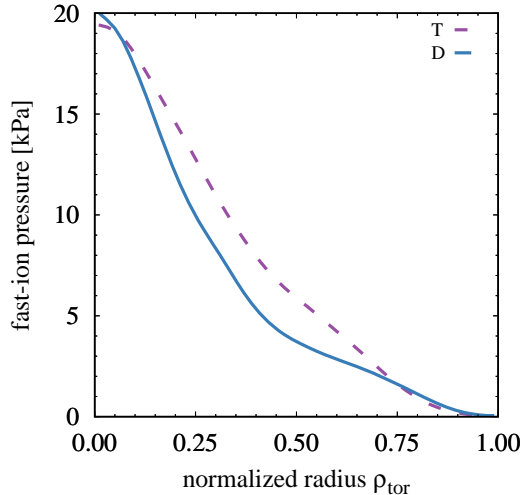


FIG. 4: Fast-ion pressure for  $P_{\text{NBI}} = 13$  MW for T-NBI into T (JPN99224) and D-NBI into D (JPN97512) at similar densities.

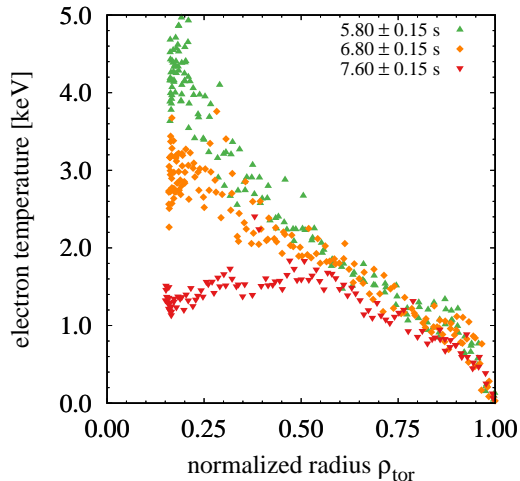


FIG. 5: Sequence of impurity accumulation in JPN96830 at  $\beta_{\text{N}} = 2.55$ : stable electron temperature profile until 6.3 s, influenced by 3/2 mode at 6.8 s, hollow  $T_e$  profile at 7.6 s.

delay between the valve opening and the gas arriving at the plasma boundary. When using TIMs the timing of the valve openings is adjusted to minimize an impact due to differences in the gas flow. Details on the impact of this time delay can be found in [39]. The auxiliary gas fuelling is adjusted depending on the plasma pressure, for moderate pressures of  $\beta_{\text{N}} \leq 2.2$  the plasmas are quite resilient against impurity accumulation and we run the gas scans with 3 different gas fuelling levels  $0.8 \cdot 10^{22}$ ,  $1.3 \cdot 10^{22}$  and  $1.8 \cdot 10^{22}$  particles/s. For higher pressures  $\beta_{\text{N}} \geq 2.5$  all of the plasmas develop MHD modes which have a negative impact on the impurity balance in the plasma [40] which can result in a negative feedback loop ending in a radiative collapse due to impurity accumulation. Such sequence is illustrated in the form of electron temperature profiles in figure 5. Until a sawtooth triggers a  $n = 3$ ,  $m = 2$  mode at 6.3 s the temperature profile is stable and peaked, then at 6.8 s the magnetic island is visible in the temperature profile between a normalized radius of 0.4-0.6. Already  $3\tau_{\text{E}}$  later so many high-Z impurities have accumulated in the core to result in a hollow  $T_e$  profile. At the magnetic field of 1.7 T no favourable source of local heating is available at JET to stop this negative feedback loop. It does not help that at these densities the T pulses tend to have less central NBI heating than their D counterparts. Therefore, in the presented experiments the impurity control is done via the gas fuelling which impacts the ELM frequency  $f_{\text{ELM}}$ . With a sufficiently high  $f_{\text{ELM}}$  the impurity flux arriving in the core is moderated down to tolerable levels. Consequently no fixed gas fuelling rates are applied

for the high  $\beta_N$  plasmas.

**Isotope purity:** For the comparison of plasmas in H, D and T the goal is to have the highest possible isotope purity which is achievable with the JET Be/W wall. However, a perfectly pure plasma is experimentally not feasible. All plasmas will have a minimum of 1-2% hydrogen which can be a legacy of H fuelling to facilitate ion cyclotron minority heating or from the H prefill gas used for the T plasmas. Some of the hydrogen plasmas presented here were performed during the D campaign, therefore, while the D was cleaned of the walls by H-D mixture experiments in advance, some residual D remained. Still a more relevant impact was the usage of D-NBI in these plasmas to achieve higher NBI power than possible with H-NBI, where technical issues limit the maximum NBI power to 10 MW [11]. This resulted in concentrations of  $n_H/(n_H + n_D) \sim 0.9$  with the hydrogen and deuterium densities  $n_H$  and  $n_D$ . Still for all metrics discussed in this paper these plasmas exhibit no differences to plasmas with higher H concentrations. For the T campaign more time was allocated to clean the vacuum vessel of residual D in order to reduce the 14 MeV neutron production to below 1%, due to D-T neutron budget restrictions for the following DTE2 campaign. Concentrations of  $n_T/(n_H + n_D + n_T) > 0.98$  were achieved. Additional to the main hydrogenic ions the plasma contains low-Z impurities which can dilute the main plasma and are mainly beryllium, carbon and neon. Due to the metallic wall the impurity content is generally quite low. We find the effective charge number  $Z_{\text{eff}}$ , as measured by visible Bremsstrahlungs spectroscopy, with  $Z_{\text{eff}} < 1.5$ . There have been some issues with the calibration of this diagnostic, however, due to the overall low impurity content the impact on the ion density profiles due to uncertainties in  $Z_{\text{eff}}$  is expected to be well below 10%. High-Z impurities like tungsten do not dilute the main plasma due to their low concentrations, however, they contribute to the radiated power as discussed below.

**Plasma shape:** Another parameter that is varied in the experiment is the plasma shape, in particular, the plasma triangularity  $\delta$  which is known to have a significant impact on the pedestal for these 1.4 MA, 1.7 T plasmas [34]. While changing the triangularity extra care was employed to keep the divertor configuration constant and the strike points in the corner position. Effectively this means only the upper triangularity is varied, while the lower triangularity remains the same. This is relevant because changing the strike point position will have a considerable impact on the fuelling characteristics [41]. The flux surfaces of the two shapes which are used in this work are illustrated in figure 6. The corresponding triangularities are low  $\delta = 0.20 \dots 0.25$  and high  $\delta = 0.29 \dots 0.32$  where the variation within each set is due to the Shafranov shift of the plasma center with different plasma pressures. Where we define the average triangularity as  $\delta = (\delta_{\text{up}} + \delta_{\text{low}})/2$  with the upper triangularity  $\delta_{\text{up}}$  and the lower triangularity  $\delta_{\text{low}}$ . Since  $\delta_{\text{low}}$  is kept constant most of the variation in the average  $\delta$  originates in changes of  $\delta_{\text{up}}$ . Note that this variation of  $\delta$ , while it has an impact on the plasma, is not comparable to the impact of a high  $\delta$  up to 0.6 in a machine like DIII-D [42]. A directly measurable impact due to the different  $\delta$  is in the particle flow balance between inner and outer divertor. Langmuir probe data suggests that the ion fluxes towards the inner divertor decrease by 10-100% with higher  $\delta$  while the fluxes to the outer divertor stay the same within the uncertainties of  $\pm 30\%$ .

**Radiation:** The core radiated power in these JET-ILW plasmas is dominated by the high-Z impurity tungsten which contributes about 95% of the total radiated power. From observations in H and D we expect the particle and thereby also the impurity confinement to increase with larger main ion isotope mass. To mimic the impurity behaviour of a plasma with a heavier isotope experiments with a lighter isotope but higher triangularity were executed. This works quite well for H and D, a high  $\delta$  H plasma has the same bulk radiated power  $P_{\text{rad,bulk}}$  as a low  $\delta$  D plasma. However, despite D and T having a smaller relative mass difference, the high  $\delta$  D plasmas designed to mimic low  $\delta$  T conditions still exhibit lower bulk radiation than their T counterparts. In figure 7 an overview is given for all three isotopes, the high  $\delta$  T plasmas partly suffer from impurity accumulation as discussed above, therefore, the scatter of  $P_{\text{rad,bulk}}$  is larger there. Despite similar auxiliary heating power, the T plasmas will have lower heat fluxes by 0.5-1.0 MW. Most of this difference is expected to originate from the edge plasma with  $\rho_{\text{tor}} > 0.7$  which accounts for 70% of the total radiated power. This is shown in figure 8 where we compare tomographic reconstructions of bolometer measurements for H and T plasmas with a pedestal density match. To take the different radiation into account we introduce the power over the separatrix

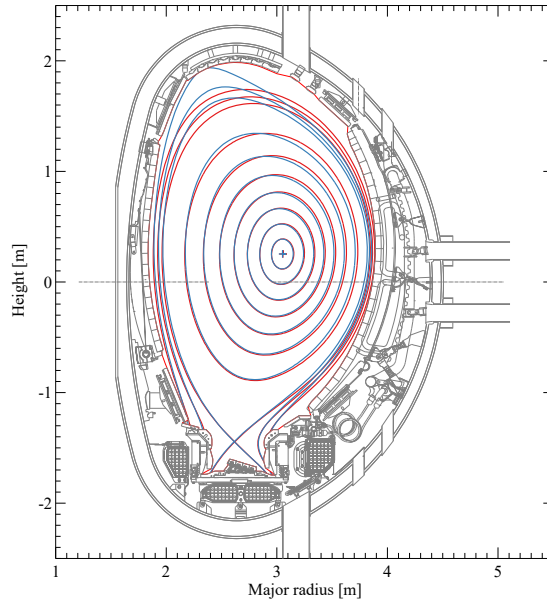


FIG. 6: High and low triangularity shapes where only the upper triangularity is varied.

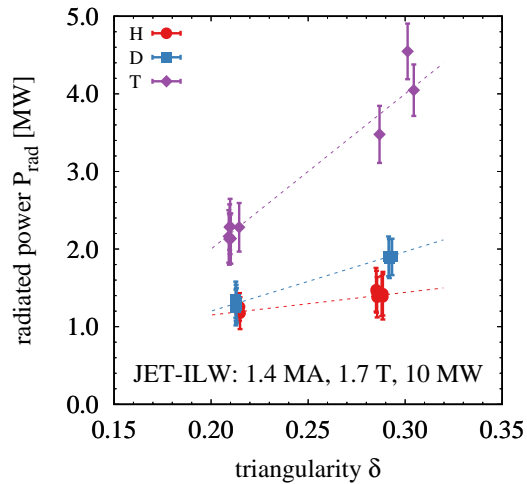


FIG. 7: Bulk plasma radiated power at different triangularities for H, D and T.

$P_{\text{sep}} = P_{\text{heat}} - \partial W/\partial t - P_{\text{rad,bulk}}$ , where  $P_{\text{heat}} = P_{\text{nbi}} + P_{\text{ohm}}$ , with  $P_{\text{ohm}}$  being the ohmic heating power, the changes in the stored energy  $\partial W/\partial t$  are negligible during the stationary phases discussed here.

### 3 Analysis procedure

**Profile diagnostics:** The main profile diagnostics utilized for this work are the Thomson scattering HRTS [43] and charge exchange spectroscopy CXRS [44]. The HRTS yields reliable electron density  $n_e$  and temperature  $T_e$  profiles up to the separatrix with sufficient time resolution to resolve ELM cycles. The core CXRS diagnostic measures the ion temperature  $T_i$  and toroidal rotation frequency  $\omega_{\text{tor}}$  of impurity ions and for selected cases also from the main ions. The main impurity used for CXRS is neon, which is puffed in small quantity during the flattop to enhance the measured CX signal. Due to the ITER like wall ILW with Be and W plasma facing components the intrinsic content of carbon is generally too low to be useful for CXRS measurements. Due to a dedicated edge CXRS system  $T_i$  and  $\omega_{\text{tor}}$  are available reliably up to the pedestal top, information about pedestal gradients and separatrix values is only available under optimal conditions which was not the case for the entire database discussed here.

**Coordinate mapping:** The profile data is mapped from real space to flux coordinates

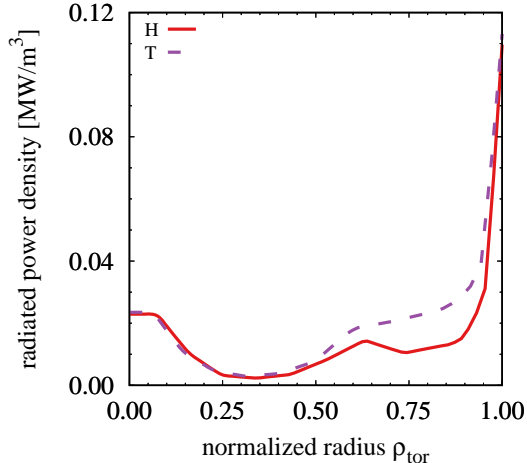


FIG. 8: Radiated power density profile for a H and T with the same auxiliary heating power at matched densities (cp. figure 42).

using equilibrium reconstructions with the EFIT code. This procedure can introduce significant uncertainties and even discrepancies, therefore, we tested the mapping of equilibria with different levels of sophistication.

The magnetics only reconstruction labeled EFIT typically underestimates the Shafranov shift of the plasma center due to the missing pressure constraints, which becomes particularly important for high  $\beta_N$  plasmas. Also the reconstructed separatrix shape is found to be inconsistent mainly below the midplane. This becomes evident in the data of diagnostics which measure below the midplane up to the separatrix like the HRTS where the profiles need to be shifted up to several cm to be consistent with the expected separatrix temperatures of  $T_{e,sep} = 100$  eV. Taking the electron pressure from HRTS measurements into account in an EFIT reconstruction is called EFTP, this improves the consistency of the equilibrium reconstruction significantly and necessary profile shifts remain below 1 cm. The EFTP reconstruction is available for all pulses and is therefore used for the coordinate mapping of measurements throughout the paper. However, the EFTP reconstruction is only based on the electron pressure while  $T_i = T_e$  is assumed and the fast-ion pressure is neglected. To test the impact of this assumption we did EFIT++ reconstructions, which utilize an iterative work flow. We map and fit the experimental profiles  $n_e$ ,  $T_e$ ,  $T_i$  using the magnetics only EFIT, then run TRANSP to determine the fast-ion pressure which then gives the best possible approximation of the total pressure profile. This is then used as input for the equilibrium reconstruction which gives the improved equilibrium EFIT++. This new equilibrium is then used to map the diagnostic data again. The results for a plasma with  $T_i > T_e$  and  $\sim 20\%$  of fast-ion content is shown in figure 9 (a) and illustrate that a significant discrepancy can arise in the core when the profiles are compared on normalized poloidal flux coordinates with  $\rho_{pol} = \sqrt{(\psi - \psi_{axis})/(\psi_{sep} - \psi_{axis})}$  where  $\psi$  is the poloidal flux and  $\psi_{axis}$  and  $\psi_{sep}$  the respective values at the magnetic axis and the separatrix. In figure 9 (b) it is shown that this discrepancy is avoided when the normalized toroidal flux label  $\rho_{tor} = \sqrt{(\phi - \phi_{axis})/(\phi_{sep} - \phi_{axis})}$  is used instead, where  $\phi$  is the toroidal flux. Therefore, we will use the normalized toroidal flux label  $\rho_{tor}$  for core profiles throughout the paper and only plot comparisons on  $\rho_{pol}$  for the pedestal where the potential discrepancy due to the missing fast-ion pressure in the EFTP equilibrium is minimal. Note that the discrepancy between EFTP and EFIT++ is expected to be most severe for high fast-ion pressures, in the shown example  $W_{fast}/W_{th} \sim 0.2$ .

We utilize an additional type of equilibrium reconstruction which relies on MHD markers like the sawtooth inversion radius or the position of a mode with known mode numbers. These MHD markers are then used in an EFTP equilibrium to constraint the q-profile and run with enhanced spatial resolution. An accurate q-profile is particularly important for the gyrokinetic simulations discussed in section 9, therefore, this type of equilibrium was used as input for the gyrokinetic simulations.

**ELM synchronisation:** If not stated otherwise all shown profiles are ELM synchronised

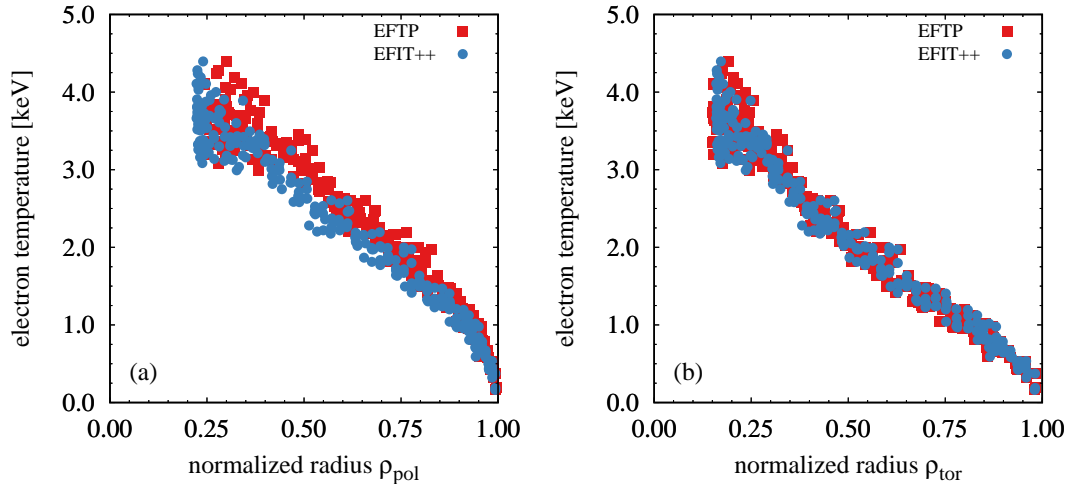


FIG. 9: Mapping of the Thomson scattering data onto flux coordinates  $\rho_{\text{pol}}$  (a) and  $\rho_{\text{tor}}$  (b) done with different equilibria for JPN99224.

and the pre ELM data is shown. The ELM synchronisation is done relative to the rise of the Be II line intensity measured in the divertor which is used as ELM indicator. All profiles are sorted in time relative to the next ELM and profiles which are within a 2-3 ms time window up to the ELM crash are selected as pre ELM. The time window will slightly vary depending on the ELM frequency  $f_{\text{ELM}}$ , the length of the available stationary phase as well as the availability of HRTS laser pulses relative to the ELMs. When ELM frequencies are shown those are also determined using the Be II radiation where the frequency is determined via the mean of the time between two adjacent ELMs  $f_{\text{ELM}} = 1/\langle\Delta t_{\text{ELM}}\rangle$ , uncertainties are then determined as one standard deviation of the  $\Delta t_{\text{ELM}}$  distribution. This means a small uncertainty of  $f_{\text{ELM}}$  corresponds to fairly regular ELMs, while a large uncertainty stems from more irregular ELMs, e.g. smaller ELMs in between more regularly occurring larger ELMs.

**Profile fitting:** The temperature and density profiles are fitted using a modified hyperbolic tangent function [45] which uses a hyperbolic tangent to fit the pedestal and is connected to a 3rd order polynomial in the core and 1st order polynomial in the scrape off layer. On the magnetic axis  $\partial f/\partial\rho_{\text{tor}} = 0$  is used as boundary condition, where  $f$  is the fit function. The angular frequency  $\omega$  is fitted using a spline with free knot locations and  $\partial\omega/\partial\rho_{\text{tor}} = 0$  on the magnetic axis, additionally, curvature changes are penalized in the very center  $\rho_{\text{tor}} < 0.2$  where the data quality tends to degrade due to low impurity content. Uncertainties on profile data are determined statistically using the distribution of experimental data over the stationary time intervals selected for analysis. No systematic uncertainties, e.g. due to diagnostic calibration, are taken into account. When determining the pedestal width and gradients we will employ a bilinear fit [46] on only the edge data. For the density this method yields similar values than an approach with modified hyperbolic tangent fit, for the temperature the values can vary. The reason for this is the relatively gradual change of the temperature inside of the steep gradient region which causes the pedestal width to vary by a factor of 2 depending on the regularisation imposed by the fit function and the radial range of experimental data included in the fit. We fit the data between  $\rho_{\text{pol}} = 0.70$  and the foot of the pedestal which is typically at  $\rho_{\text{pol}} \simeq 1.01$ . The pedestal width  $\Delta$  is then defined as the distance from the pedestal top to separatrix.

**Doppler reflectometry:** The power measured by with a reflectometer using a Doppler backscattering DBS technique can be a proxy for the density fluctuation level  $\tilde{n}/n$  at the scattering layer in the plasma [47]. We are using the correlation reflectometer [48] for this purpose by utilizing only the main probing frequencies  $f_{\text{probe}}$ . This is the Doppler V-band with frequencies of 48.8...74.0 GHz in X-mode. One full sweep takes 286 ms covering 14 distinct frequencies in this range. At the magnetic field of 1.7 T this correspond to densities of  $\sim 1.2...3.0 \cdot 10^{19} \text{ m}^{-3}$  as determined with ray tracing. This means at low densities we probe the plasma from inside the pedestal top, over the steep gradient region

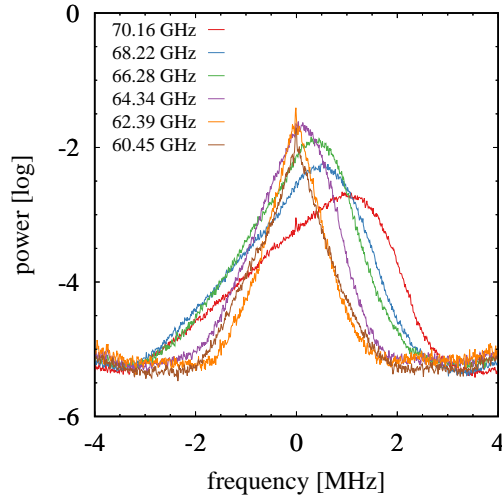


FIG. 10: Measured power spectra by Doppler reflectometry for different probing frequencies.

nearly up to the separatrix. Measured power spectra for different probing frequencies are shown in figure 10. While we see a clear Doppler shift when probing the plasma inside of the pedestal top, the Doppler peak vanishes for  $f_{\text{probe}}$  corresponding to the steep gradient region. Only a relatively symmetric spectrum remains around zero frequency. This can be explained by the very low turbulence levels in the steep gradient region which result in a very low backscattered signal and allows signals from other sources to dominate the spectrum. The source for the peak at zero frequency or zero rotation is most likely due to normal incidence reflection from the plasma. Despite operating the reflectometer with the main microwave beam tilted relatively to the flux surfaces to obtain backscattering there can be components with normal incidents. This is either due to a wide main lobe or due to side lobes and commonly observed for Doppler reflectometry [49]. Although, these components are typically attenuated by 10 dB or more below the main lobe, the turbulence level is higher at the normal incidence with  $k_{\perp} \sim 0 \dots 1 \text{ cm}^{-1}$  compared to the expected Doppler  $k_{\perp} \sim 10 \dots 15 \text{ cm}^{-1}$  by at least 10 dB. To characterise the spectral power we fit the spectra using a Gaussian parametrisation for each time point and then average over the inter ELM phases for each frequency.

## 4 Coupling between transport channels and transport regions

### 4.1 Pedestal transport model

As discussed in the introduction the consistent treatment of the different transport channels and their interdependence is important. Therefore, we built a transport model using only very basic well known physics constraints. The novelty in our approach is that we implement those constraint in a coupled self consistent source driven full radius model including heat and particle transport channels. The model is run within the ASTRA code which also captures the temporal evolution. This allows us to understand trivial dependencies, which otherwise might be obscured by the complexity of the non-linear interactions between the transport channels. The purpose of the model is not to predict plasma parameters but to illustrate the chain of consequences that changes will set off in a coupled environment such as a fusion plasma. The physics ingredients of the model are

- A critical gradient model [50] determines the heat diffusivity  $\chi$  over the full radius up to the separatrix.
- A pedestal transport constraint reduces the heat diffusivity when the local  $\gamma_{E \times B}$  exceeds a critical shearing rate. A mass dependence can be introduced in the diffusivity.
- The particle diffusivity is coupled to the ion heat diffusivity over the full radius.

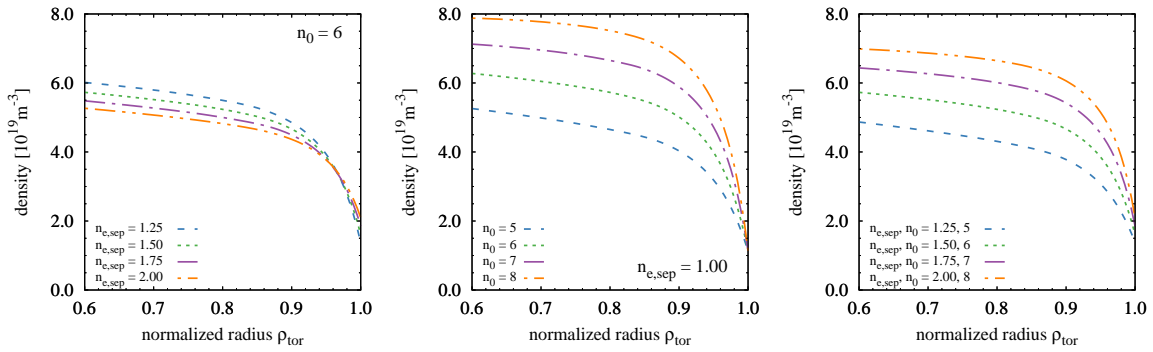


FIG. 11: Expected influence of neutral penetration on the density profile in transport equilibrium, when varying separatrix density (a), neutral flux (b) or both (c).

- A 1D neutral penetration model [51] calculates the particle source taking the ion mass into account.
- An ELM cycle model is used which triggers a short (1 ms) phase of enhanced transport when the maximum in the normalized pressure gradient  $\max(\alpha)$  exceeds a predetermined critical value  $\alpha_{\text{crit}}$ .

The necessary coefficients and critical values are chosen with existing studies in mind but ultimately arbitrarily to reproduce physically reasonable profiles and then scanned successively to document their impact. We distinguish between two general applications of the model, the full model including ELM cycles and a transport limited case where  $\alpha_{\text{crit}}$  is chosen so high that no ELMs are triggered. Note that results from transport limited modelling often do not hold when ELMs are introduced, however, they help to understand the impact of changes in such a coupled system.

The most important ingredient in the model is the transport mitigation above a critical shearing rate  $\gamma_{E \times B}$  which allows us to reproduce H-mode like profiles with steep gradients in the edge. The width of this pedestal is determined by neutral penetration which acts as seed for the electric field well that is responsible for the shearing rate. The pedestal is then formed by the nonlinear cycle of transport mitigation due to  $\gamma_{E \times B}$ , steeper gradients due to lower transport and consequently higher  $\gamma_{E \times B}$ .  $\max(\alpha)$  will reach an equilibrium  $\alpha_{\text{eq}}$  in the transport limited case because we impose a radial smoothing of the diffusivity to prevent local singularities. In the full ELM cycle case this would not be necessary as the gradients are limited by the imposed  $\alpha_{\text{crit}}$ .  $\alpha_{\text{eq}}$  will depend on the transport coefficients and the heat and particle sources.

Since we only simulate up to the separatrix we need to set the separatrix values  $T_{e,\text{sep}}$ ,  $T_{i,\text{sep}}$  and  $n_{e,\text{sep}}$  as boundary condition. Consequently, the question arises on how to treat gas fuelling in the model. Due to the direct influence of  $n_{e,\text{sep}}$  on  $\gamma_{E \times B}$  it makes a huge difference whether  $n_{e,\text{sep}}$  and the neutral flux  $\Gamma$  are changed individually or together. In the model the neutral flux is introduced via neutrals  $n_0 [10^{15} \text{m}^{-3}]$  with a fixed energy of 5 eV. The results of scans in  $n_{e,\text{sep}}$  and  $n_0$  are shown in figure 11 for the density and in figure 12 for the pressure. Increasing  $n_{e,\text{sep}}$  reduces  $\gamma_{E \times B}$  and will result in higher transport and consequently lower density and pressure. Increasing  $n_0$  or  $\Gamma$  increases  $\nabla n_e$  and therefore  $\gamma_{E \times B}$  and will reduce transport and increase density and pressure. Modifying both at the same time will increase the density at constant pressure. This illustrates an important concept which we will call fuelling efficiency. It describes the efficiency of depositing particles within the plasma while keeping  $n_{e,\text{sep}}$  constant. The fuelling efficiency is different to general fuelling where  $n_{e,\text{sep}}$  and  $\Gamma$  change simultaneously. Improving the fuelling efficiency will be beneficial for confinement while normal fuelling can have a detrimental impact.

In the neutral penetration model the ion mass plays an important role and a lower mass will result in higher densities due to deeper neutral penetration. Since this is opposite to experimental observations, we allow for a mass dependence in the edge transport. In figure 13 different cases are shown with  $\chi \propto A^\mu$  where  $\mu = -1, -\frac{1}{2}, 0$ . A linear dependence on the ion mass is required to reverse the density dependence. Note that the changes in the transport model due to the mass are enhanced by the self consistently calculated  $\gamma_{E \times B}$ . In

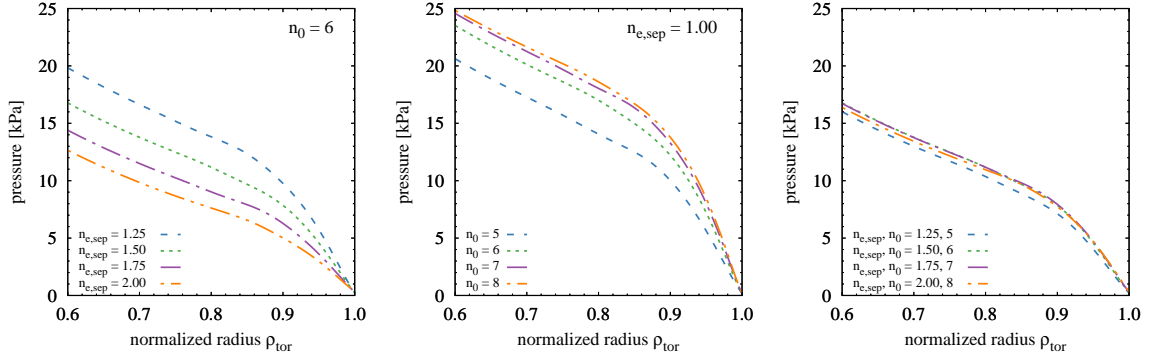


FIG. 12: Expected influence of neutral penetration on the pressure profile in transport equilibrium, when varying separatrix density (a), neutral flux (b) or both (c).

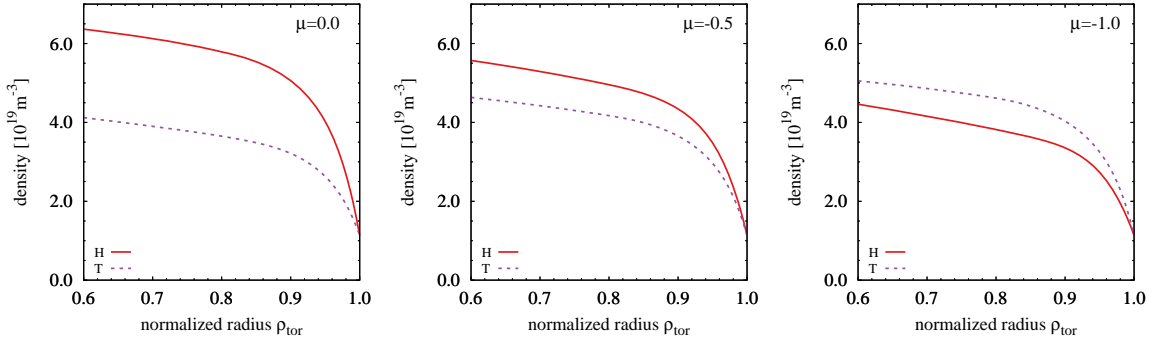


FIG. 13: Expected influence of a mass dependence in edge heat and particle transport with  $\chi \propto A^\mu$  on the pedestal density in the transport limited case.

the case without mass dependence ( $\mu = 0$ ) H would have a  $\sim 70\%$  higher pedestal pressure than T while with mass dependence ( $\mu = -1$ ) H does not even reach half of the pressure found in T. The profiles are shown in figure 14 and highlight the strong impact of a mass dependence in the pedestal transport.

When using  $\mu = -1.0$  for the edge diffusivity, we find that, for lower mass or higher transport, changes in the fuelling efficiency play a more important role. This is illustrated in figure 15 where  $\alpha_{\max}$  in equilibrium is plotted against the neutral flux for different masses and  $n_{e,\text{sep}}$ . In the model the hydrogen case with higher transport falls back to L-mode like profiles while tritium retains a pedestal for the same inputs. The relative impact of the fuelling efficiency is plotted as the variation of the pedestal pressure  $p_{\text{ped}}$ . For low transport - i.e. T and low  $n_{e,\text{sep}}$  - the change of  $p_{\text{ped}}$  is negligible while it can be over a factor of 2 for high transport - i.e. H and high  $n_{e,\text{sep}}$ . The impact of the fuelling efficiency propagates via  $\gamma_{E \times B}$  turbulence mitigation in the edge, consequently, it should have no effect in regimes

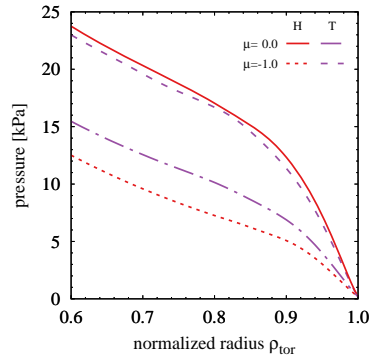


FIG. 14: Expected influence of a mass dependence in edge heat and particle transport with  $\chi \propto A^\mu$  on the pedestal pressure in the transport limited case.

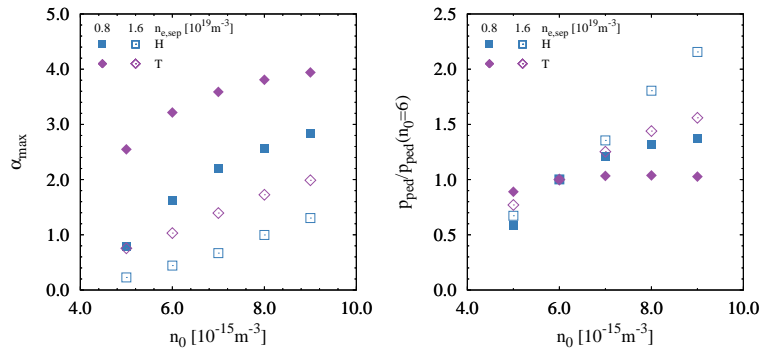


FIG. 15: Overview of  $\alpha_{\max}$  (a) and relative pedestal pressure changes (b) in transport equilibrium with mass dependent  $\mu = -1$  heat and particle transport for different neutral flux, separatrix density and main ion mass.

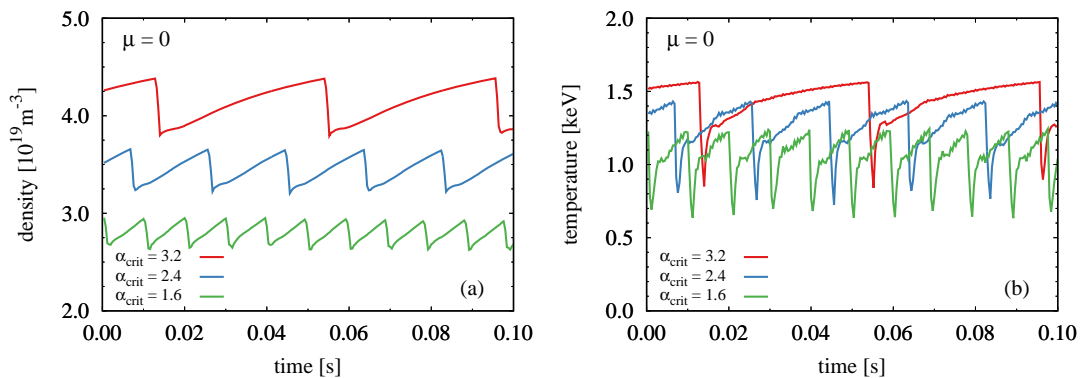


FIG. 16: Evolution of density (a) and temperature (b) during an ELM cycle at  $\rho_{\text{tor}} = 0.92$  for different  $\alpha_{\text{crit}}$  and an  $\alpha_{\text{eq}} = 3.8$ .

where this mechanism of turbulence mitigation is not relevant - like in L-mode plasmas.

The transport limited simulations are of educational value as they illustrate basic nonlinear interactions between the particle and heat transport channels. However, those steady state solutions are likely not stable against peeling ballooning modes and when ELMs are the limiting factor the results can change significantly. To illustrate the basic features of these ELMy simulations we start with a transport limited,  $\mu = 0$  case with an  $\alpha_{\text{eq}} = 3.8$ , activate the ELM crash model by having  $\alpha_{\text{crit}} < \alpha_{\text{eq}}$  and vary  $\alpha_{\text{crit}}$  below this upper bound. The result of this  $\alpha_{\text{crit}}$  scan is shown in figure 16, for lower  $\alpha_{\text{crit}}$  the pedestal density and temperature are naturally lower just before the crash, where the density varies more than the temperature. Additionally, the ELMs become smaller and more frequent. The reason for the higher  $f_{\text{ELM}}$  stems from the non-linearity of the  $\gamma_{E \times B}$  transport model which is best visible in the temperature recovery time traces. After the crash the pedestal is near instantaneously refilled with energy from the core which help to start the bootstrap loop of increasing  $\gamma_{E \times B}$  and thereby reducing transport, followed by steepening of gradients which in turn increase  $\gamma_{E \times B}$ . This process slows down as  $\alpha_{\max}$  approaches the transport equilibrium  $\alpha_{\text{eq}}$ . The reason for the difference in ELM size is not directly obvious, as the coefficients for the enhanced transport during the 1 ms ELM crash are the same in all cases. This shows how the ELM frequency can change despite constant heat and particle sources. In this picture the change of the ELM frequency with different heat and particle sources is a result of  $\alpha_{\text{eq}}$  and  $\alpha_{\text{crit}}$  changing at different rates. In experiment type-I ELMs increase in frequency for higher heating power and higher heating power should result in higher  $\alpha_{\text{eq}}$ . In figure 17 the change of  $f_{\text{ELM}}$  with  $\alpha_{\text{eq}}/\alpha_{\text{crit}}$  is shown for an  $\alpha_{\text{crit}}$  scan where  $\alpha_{\text{eq}} = 3.8$ .

The impact of a mass dependence in the edge transport model is illustrated for ELM limited cases in figure 18. We find that the mass dependence in the edge transport model has very little impact on the pedestal density and temperature. The main impact is visible in  $f_{\text{ELM}}$  which changes according to the impact on  $\alpha_{\text{eq}}$ , increased transport yields a lower  $f_{\text{ELM}}$  in H and reduced transport yields a higher  $f_{\text{ELM}}$  in T. Due to the same  $\alpha_{\text{crit}} < \alpha_{\text{eq}}$  the pedestal

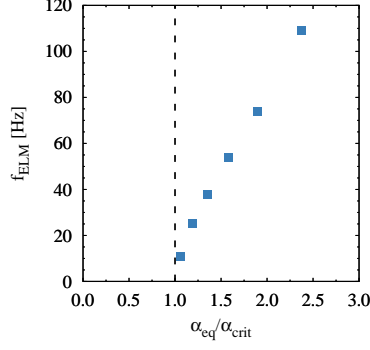


FIG. 17: ELM frequency as a function of  $\alpha_{\text{eq}}/\alpha_{\text{crit}}$ .

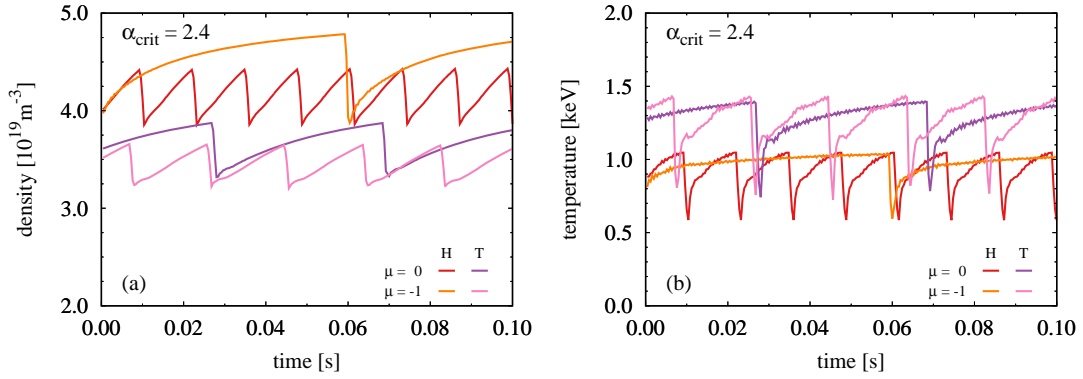


FIG. 18: Evolution of density (a) and temperature (b) during an ELM cycle at  $\rho_{\text{tor}} = 0.92$  for the same  $\alpha_{\text{crit}}$  but different mass dependence in the edge transport model for H and T.

pressure is the same for H and T, while the mass dependent neutral penetration results in a higher density for lower mass.

Since the transport model discussed here is based on coupled heat and particle transport changing  $\alpha_{\text{crit}}$  will not vary the ratio  $n/T$ . A way to vary  $n/T$  at constant  $\alpha_{\text{crit}}$  is via the particle sources or the fuelling efficiency  $n_0$  as discussed above. Such a  $n_0$  variation is illustrated in figure 19. While changing the diffusivities via the mass exponent  $\mu$  again only results in different  $f_{\text{ELM}}$ , a reduction of the neutral source  $n_0$  will significantly impact  $n/T$  at constant pressure. A similar effect could be achieved by decoupling heat and particle transport in the model.

Combining the effects discussed above we can construct a scenario where  $\alpha_{\text{crit}}$  and  $n_0$  vary with main ion isotope mass in such a way that the density is higher in T compared to D and the temperature is the same for H and T. This is illustrated for the time traces of ELM cycles in figure 20 and for edge profiles in figure 21. In this particular scenario the pedestal density and temperature before the ELM crash will reach the same values regardless of a

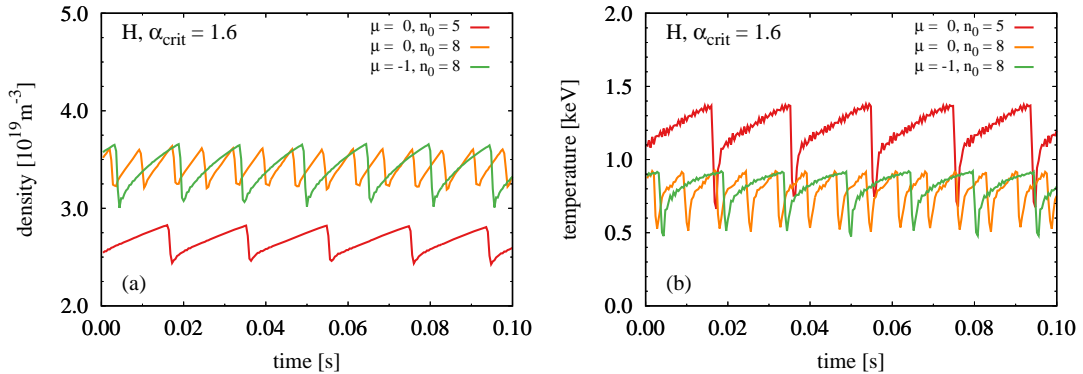


FIG. 19: Evolution of density (a) and temperature (b) during an ELM cycle at  $\rho_{\text{tor}} = 0.92$  for the same mass but different mass dependence in the edge transport model and different fuelling efficiency.

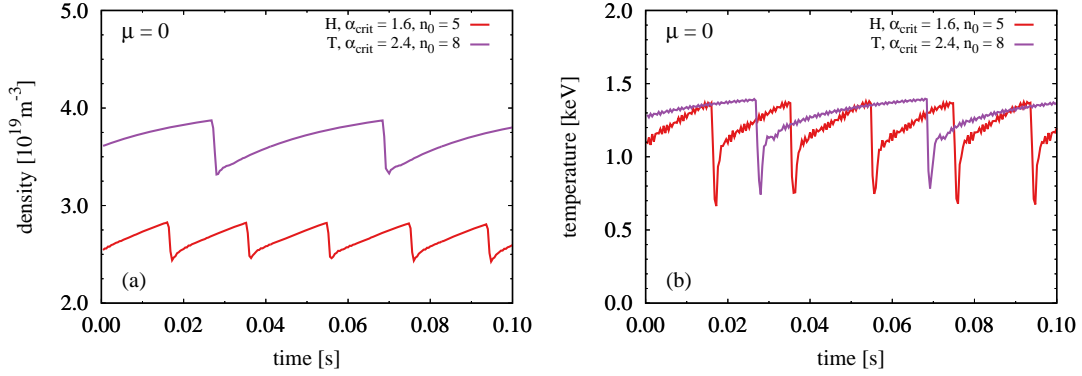


FIG. 20: Evolution of density (a) and temperature (b) during an ELM cycle at  $\rho_{\text{tor}} = 0.92$  for H and T with different  $\alpha_{\text{crit}}$  and  $n_0$ , but without any mass dependence in the transport.

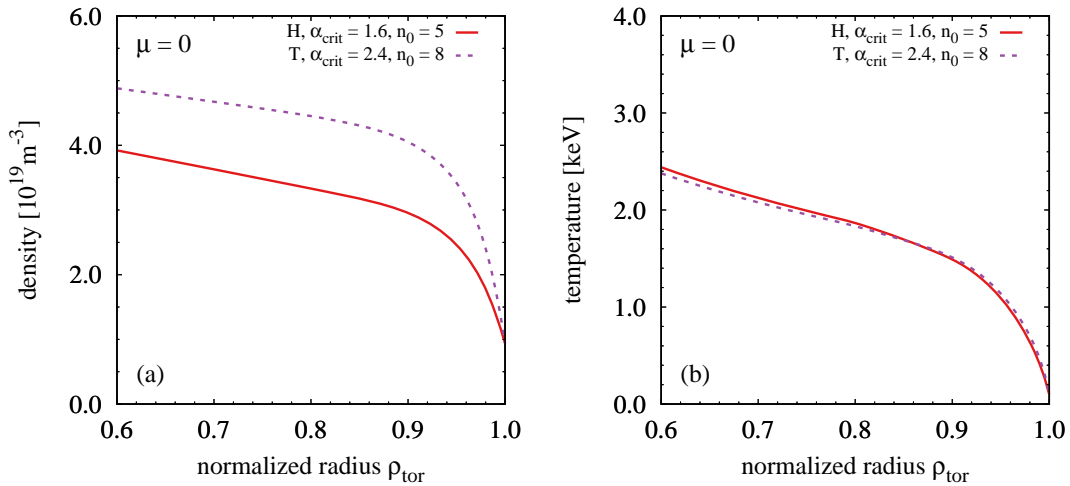


FIG. 21: Edge profiles of density (a) and temperature (b) before an ELM crash for H and T with different  $\alpha_{\text{crit}}$  and  $n_0$ , but without any mass dependence in the transport.

mass dependence in the heat and particle transport. The impact of the mass dependence in the transport is found in the ELM frequency. For our example case with  $\mu = 0$  shown here  $f_{\text{ELM}}^H/f_{\text{ELM}}^T = 2$  and with increasing mass dependence  $\mu < 0$  this ratio reduces. With  $\mu = -0.5$  the ELM frequencies are the same for H and T. For  $\mu \leq -0.75$  the simulation with otherwise the same parameters would yield an L-mode for H, i.e.  $\alpha_{\text{eq}} < 1.6$ . The parameter which is not varied here is the separatrix density which would have an additional impact if it is significantly different for H and T. However, a change of  $n_{\text{e,sep}}$  would not affect  $n/T$  in the pedestal significantly since in our model heat and particle transport are coupled.

The key result is: when an ELM stability limited pedestal ( $\alpha_{\text{crit}} < \alpha_{\text{eq}}$ ) is modelled with coupled heat and particle transport a mass dependence in the transport will not impact the profiles, only the ELM frequency. To change the profiles one can introduce a mass dependence in the sources or the heat and particle transport require different mass dependencies.

## 4.2 Core-edge coupling

In an H-mode plasma it is often assumed that transport regions core and edge can be treated independently. This is not too bad of an assumption when both core and edge parameters are not varied a lot. However, for the data set discussed here this is certainly not the case as the pedestal pressure is varied by a factor of 4 and the total pressure by a factor of 3. A known route how the global pressure can influence the edge is via  $\beta$  stabilisation of peeling-ballooning modes [52], this is taken into account in the stability analysis presented in section 6. The edge pedestal itself will again influence the core plasma and the resulting non-linear interaction can create complex feedback loops which were e.g. discussed in [6] and are one of the main motivation for integrated modelling codes like IMEP which also treat the scrape of layer [53]. For the interpretation of the parameter dependencies in our data set it will be essential to understand the leading contribution that a variation of the edge parameters will have on the core plasma. An important contribution stems from the temperature scale length invariance or profile stiffness [54]. In the limit of infinite stiffness we have  $\nabla T/T = L_T^{-1} = \text{const}$  which directly gives  $T_{\text{core}} \propto T_{\text{ped}}$ .

Another contribution is due to the temperature dependency in the efficiency of turbulent transport. This is generally associated with a gyroBohm or Bohm scaling of turbulent transport. Depending on plasma regime and species the turbulence scaling is often observed to be different [55]. However, all scalings exhibit a strong positive temperature dependence. This means for a higher temperature a larger absolute amount of heat can be transported with the same turbulent drive. Typically, the heat flux  $q$  is then normalized to the turbulence efficiency, in most cases, the gyroBohm heat flux  $q_{\text{gB}}$  or gyroBohm factor. For a purely gyroBohm like turbulent transport the normalized heat flux  $q/q_{\text{gB}}$  should be constant for a given turbulent drive  $\nabla T/T$ . For hotter plasmas the normalised heat flux goes down and less turbulent drive is required to transport the heat out of the plasma. In this case a higher pedestal temperature will result in a lower core contribution to the total pressure. For the thermal stored energy  $W_{\text{th}}$  we define the core  $W_{\text{th,core}}$  and pedestal  $W_{\text{th,ped}}$  as  $W_{\text{th}} = W_{\text{th,ped}} + W_{\text{th,core}}$ .

In a realistic plasma the transport is neither infinitely stiff nor does it purely scale like gyroBohm, therefore, we utilize the transport model TGLF-SAT2 to quantify the edge-core coupling expected for these two contributions. For this purpose we run source driven simulations of  $n_e$ ,  $T_e$  and  $T_i$  within the transport code ASTRA and the boundary fixed at  $\rho_{\text{tor}} = 0.85$ . This boundary condition is motivated by one of the T plasmas that will be discussed in the next sections. We vary the boundary condition while keeping the heat and particle sources constant. At 3 distinct pressure levels we vary the collisionality by scaling temperature and density, which results in 9 different cases which are illustrated in figure 22. The impact of the stiffness and the gyroBohm factor partly cancel each other therefore a variation of factor of 3 in the pedestal pressure only results in 40-60% increase in the core stored energy. At constant pressure the impact of a lower temperature is more obvious as a variation of a factor of 2 also yields an increase of  $W_{\text{th,core}}$  by about 50%. The correlation of the turbulent drive with the temperature is illustrated in figure 23 (a) and shown for full profiles in figure 23 (b).

To illustrate the significance of the impact the pedestal parameters have on the core transport we compare this to the impact of the main ion mass. ASTRA/TGLF-SAT2 is run with

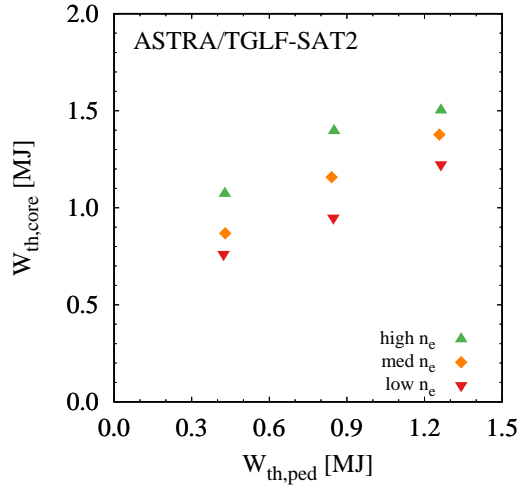


FIG. 22: Impact of boundary condition on core stored energy  $W_{\text{th,core}}$  in ASTRA/TGLF-SAT2 simulations when varying  $n_{\text{ped}}$  and  $T_{\text{ped}}$ .

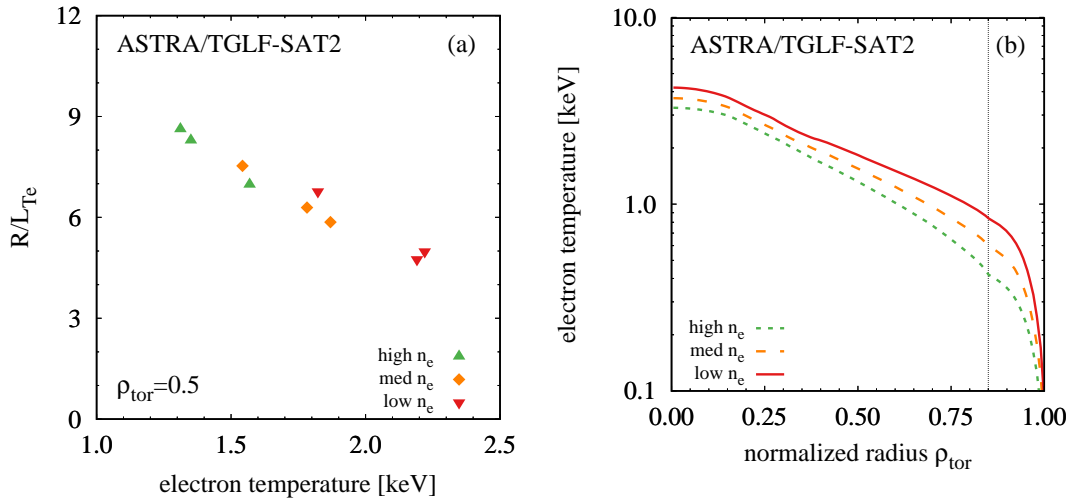


FIG. 23: Impact of variations in  $T_{\text{ped}}$  on the normalized temperature gradient length  $R/L_T$  for the whole scan at mid radius (a) and radial profiles for the low pressure cases (b).

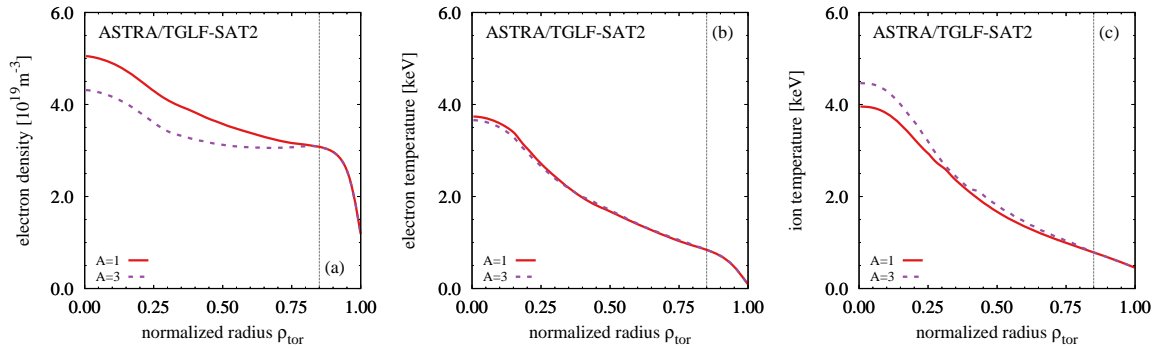


FIG. 24: Electron density (a), electron temperature (b) and ion temperature (c) profiles calculated with ASTRA/TGLF-SAT2 for different main ion masses from a boundary at  $\rho_{\text{tor}} = 0.85$ .

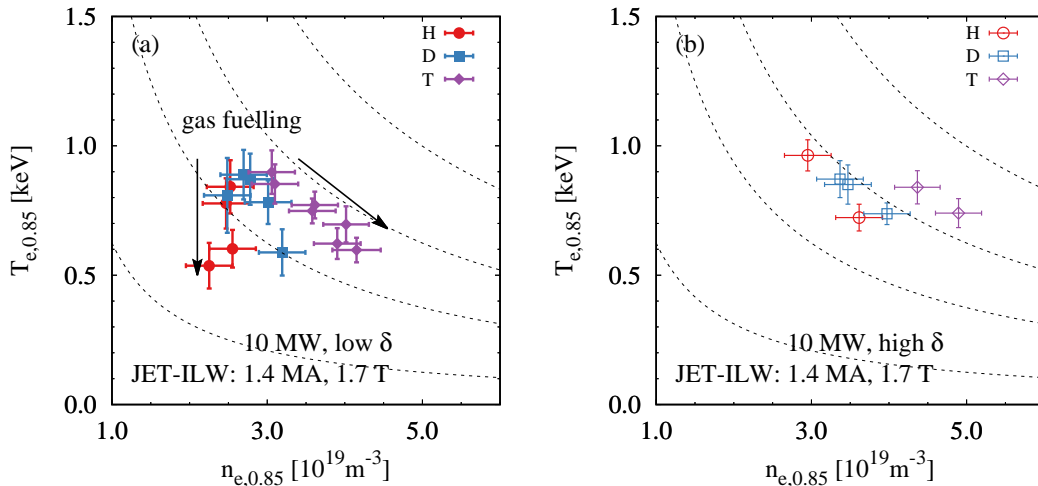


FIG. 25: Edge electron temperature - determined at  $\rho_{\text{tor}} = 0.85$  - plotted against the electron density at the same position for different main ion isotope masses and gas fuelling, but otherwise identical engineering parameters. In (a) the low  $\delta$  data is plotted and in (b) the one at high  $\delta$ . The dashed lines are isobars at 1, 3, 5 and 8 kPa.

$A = 1$  and  $A = 3$  using the average parameters of the boundary scan. The resulting profiles are shown in figure 24. We find a stronger density peaking with lower mass which has been theoretically explained by a stronger turbulent particle pinch for the lighter isotope [56]. The temperatures are fairly similar with the only differences being due to the mass dependence in the electron-ion equipartition. Since  $T_i > T_e$  more heat will end up in the electron channel for lower mass, which is the reason for the reversal of ion and electron temperatures with ion mass. Overall increasing the mass by a factor of 3 results in 19% reduction in the core stored energy which corresponds to a mass scaling suggested by TGLF-SAT2 of  $W_{\text{th,core}} \propto A^{-0.156}$ .

## 5 Pedestal characteristics

**Overview:** We have two main sets of data in H, D and T, one at high  $\beta_N = 2.5 \dots 3.0$  and one at medium  $\beta_N = 1.4 \dots 2.5$ . The aim of the first one is to obtain a comparison at high  $\beta_N$  with different isotopes and heating powers between 12 and 15 MW. At 10 MW of heating and medium  $\beta_N$  we have more operational flexibility and scan gas puff and triangularity. For the latter data set also a few DT pulses close to a ratio of  $n_D/n_T \sim 50/50$  are available, although, only at constant low gas puff.

The gas puff scan at 10 MW of heating and low  $\delta$  is shown in figure 25 (a) and significant differences between the three isotopes are observed. While for T the gas scan increases the density at constant pressure, the increase of density in D is accompanied by a reduction in pedestal pressure. In hydrogen the impact of the gas puff does not result in a higher density at the pedestal top, but in the temperature and pressure dropping significantly. This is evidence for a strong isotope mass dependence in the pedestal. This isotope mass dependence does not follow a simple power law. If we were to express the mass dependence of the density at low gas fuelling as a power law it would yield  $n_e \propto A^{0.13}$  while at high gas fuelling we find  $n_e \propto A^{0.39}$ . From figure 25 (a) it is also evident that both scalings are significantly different. Such a deviation from a single power law description is also observed when varying the triangularity. At high  $\delta$  the pressure remains constant with gas fuelling for all three isotope masses. This is quite different from the observation at low  $\delta$ , consequently, the clear isotope mass dependence that was observed at low  $\delta$  is not observed anymore. While at high  $\delta$  the T pedestal is still found at higher pressures compared to H and D, the pressure differences between H and D are negligible, despite the larger mass ratio. Note that at high  $\delta$  H and D pulses are found with a similar pedestal density and temperature compared to the low  $\delta$  T pulses, which will become important for the comparisons in the core.

At high  $\beta_N$  the interpretation of the overview plot of edge temperature and density, shown

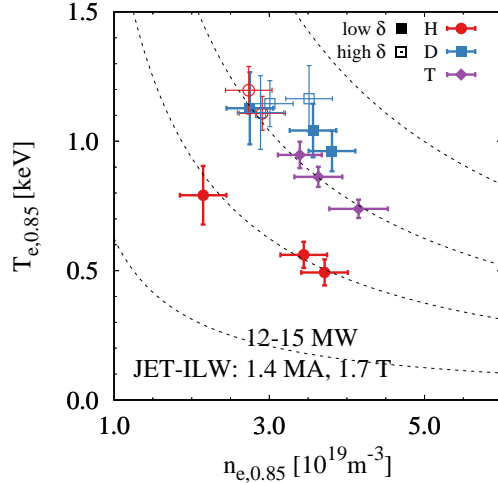


FIG. 26: Edge electron temperature - determined at  $\rho_{\text{tor}} = 0.85$  - plotted against the electron density at the same position for the high pressure data set with different main ion masses. The dashed lines are isobars at 1, 3, 5 and 8 kPa.

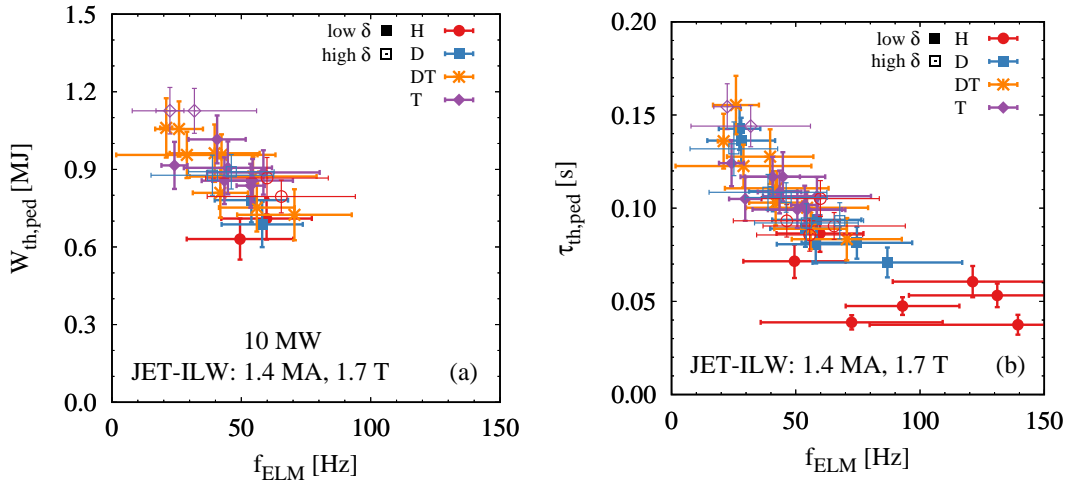


FIG. 27: Pedestal stored energy (a) and pedestal confinement time (b) plotted against the ELM frequency for 10 MW plasmas in (a) and the whole database in (b).

in figure 26, is not as straightforward because we vary heating power, gas and shape at the same time. The main goal to match temperature and density at the pedestal top for all three isotopes was not achieved, however, we have a pair at constant pressure and one at constant density. High pressure H plasmas are only achieved at high triangularity and with D-NBI, the low pressure H points reached the heating powers above 10 MW with H-NBI and ICRF heating and had low  $\delta$ .

A very strong correlation is observed between the pedestal pressure and the ELM frequency. Figure 27 (a) shows for a subset of the database at 10 MW that at lower pedestal pressure the highest  $f_{\text{ELM}}$  are found. For the whole database a similar correlation between  $f_{\text{ELM}}$  and the pedestal confinement time  $\tau_{\text{E,ped}} = W_{\text{th,ped}}/P_{\text{sep}}$  is visible in figure 27 (b). No clear separation between the isotope masses is observed in this correlation, although, the lowest pedestal confinement and highest  $f_{\text{ELM}}$  are plasmas with H as main ions which also have the most irregular ELM frequency.

**Density profiles:** The pedestal electron density profiles for the gas scan at 10 MW and low  $\delta$  are shown for H, D and T main ions in figure 28. Most striking is the density response in H, where an increase in  $n_{\text{e,sep}}$  with higher gas fuelling is observed, while the pedestal top density is effectively unchanged. In D and T gas fuelling increases the pedestal top density while the separatrix density appears to be less affected than in H, then the increase

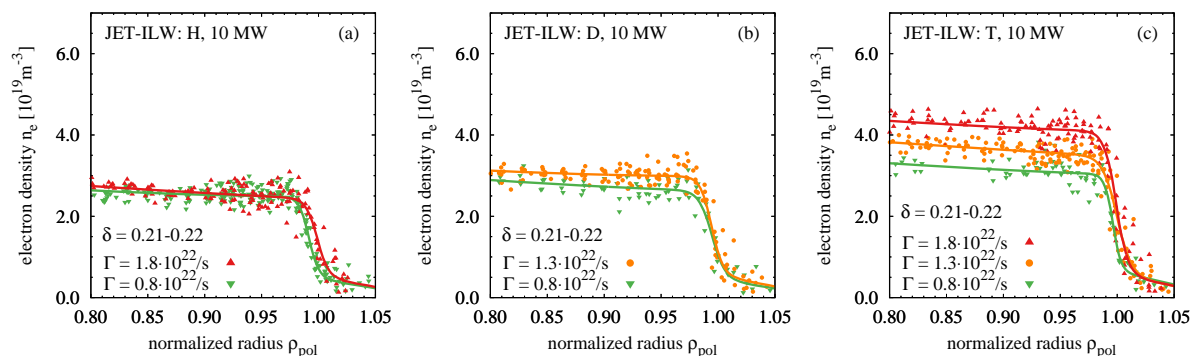


FIG. 28: Edge electron density profiles at low  $\delta$  for different gas puff levels and main ion mass: H (a), D (b) and T (c). H: JPN97094, JPN97095; D: JPN97035, JPN97036; T: JPN98794, JPN98795, JPN100177

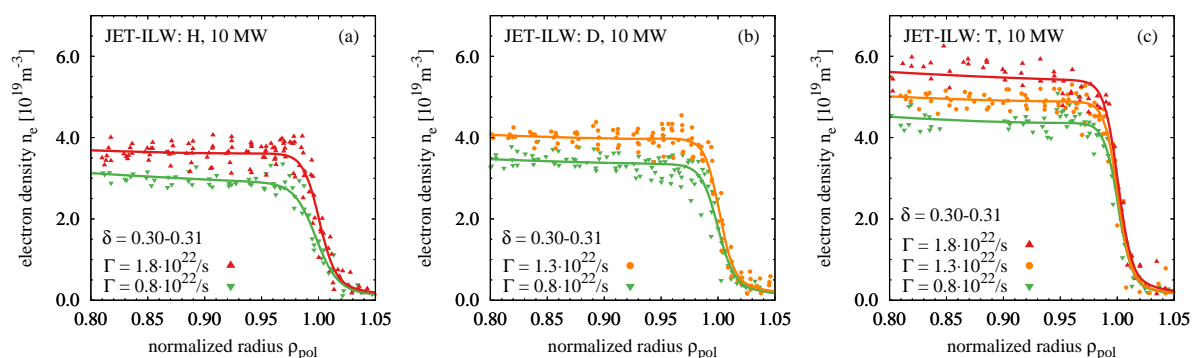


FIG. 29: Edge electron density profiles at high  $\delta$  for different gas puff levels and main ion mass: H (a), D (b) and T (c). H: JPN97094, JPN97095; D: JPN97035, JPN97036; T: JPN98794, JPN98795, JPN100177

in pedestal top density is a result of steeper gradients. In D the data would support this, for T it is not directly evident. Overall, at low  $\delta$  the changes in  $n_{e,\text{sep}}$  and  $\nabla n_e$  are not sufficient - given the available data quality - to pinpoint the cause for the pedestal top density values. This is different at high  $\delta$ , as shown in figure 29 where the higher pedestal top density with larger gas fuelling is clearly a result of steeper density gradients, while the density at the foot of the pedestal remains relatively unchanged. In particular, it is surprising that the density is constant outside of the steep gradient region for all isotope masses despite a variation in gas puff of over a factor of 2. In the picture of the pedestal transport model discussed in section 4.1 this would correspond to an improved fuelling efficiency and higher particle capacity at high  $\delta$ . Note that for our database only data from Thomson scattering is available which has relatively large uncertainties at low densities. Measurements of the Li-beam diagnostic which would improve the accuracy of the SOL data where not available for the full data set.

**Temperature profiles:** The temperature response to the changes of gas fuelling is quite similar for different  $\delta$ , as shown in figure 30 for the low  $\delta$  plasmas and in figure 31 for high  $\delta$  ones. In particular, for H, even at constant pedestal top density, the temperature drops with increasing gas puff as shown in figure 30 (a). For all three isotopes the temperature changes are comparable and scale with the gas fuelling level, although the changes in density were different for all isotopes. All the changes in the temperature pedestal top due to gas puffing are a result of different temperature gradients. There are no indications for a significant impact due to the pedestal width.

**Impact of the isotope mass:** When plotting engineering matched plasmas at high  $\delta$  with all three isotopes as done in figure 32 for high  $\delta$  it becomes evident that the density pedestal width shrinks while its gradient increases when the mass number increases. At the same time the temperature pedestal seems to be the same within the uncertainties for all three isotopes. However, the uncertainties are quite high since the temperature does not feature a similarly pronounced pedestal top as observed in the density. The transition between steep

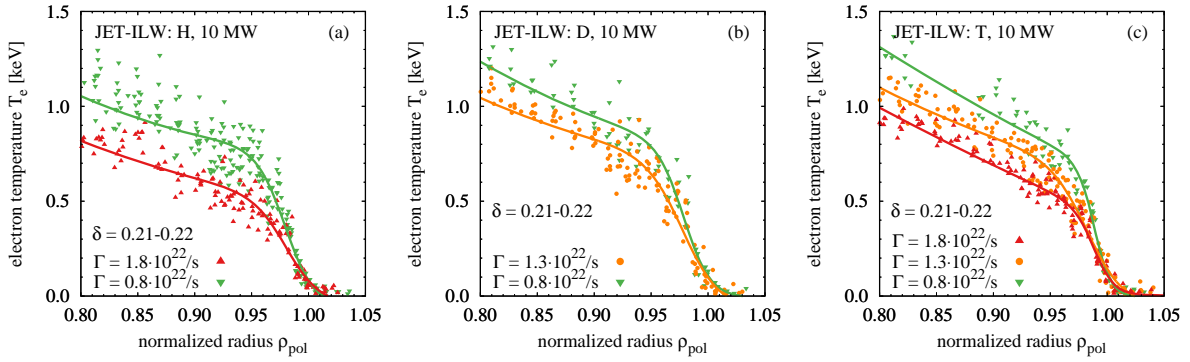


FIG. 30: Edge electron temperature profiles at low  $\delta$  for different gas puff levels and main ion mass: H (a), D (b) and T (c). H: JPN97094, JPN97095; D: JPN97035, JPN97036; T: JPN98794, JPN98795, JPN100177

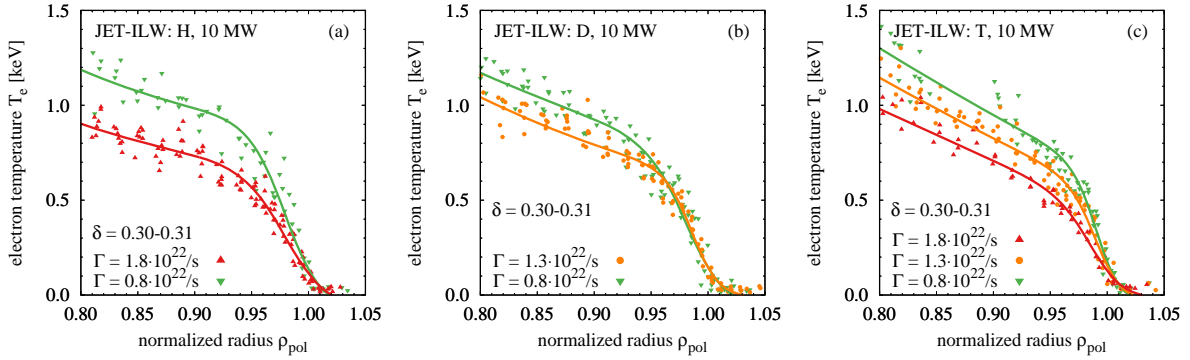


FIG. 31: Edge electron temperature profiles at high  $\delta$  for different gas puff levels and main ion mass: H (a), D (b) and T (c). H: JPN97094, JPN97095; D: JPN97035, JPN97036; T: JPN98794, JPN98795, JPN100177

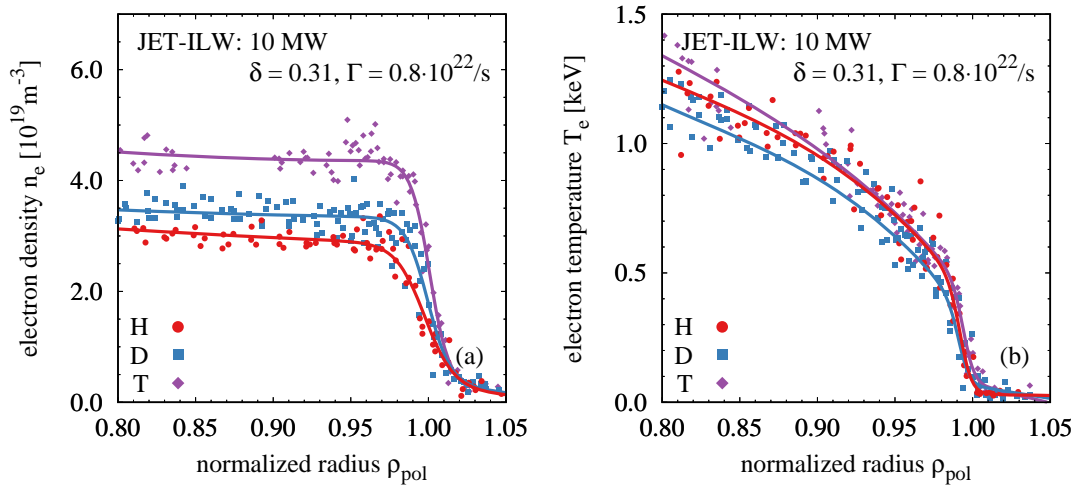


FIG. 32: Edge electron density (a) and electron temperature (b) profiles of plasmas with different main ion mass H, D, T for 10 MW of heating, high  $\delta$  and low gas puff. H: JPN97095; D: JPN97036; T: JPN98795

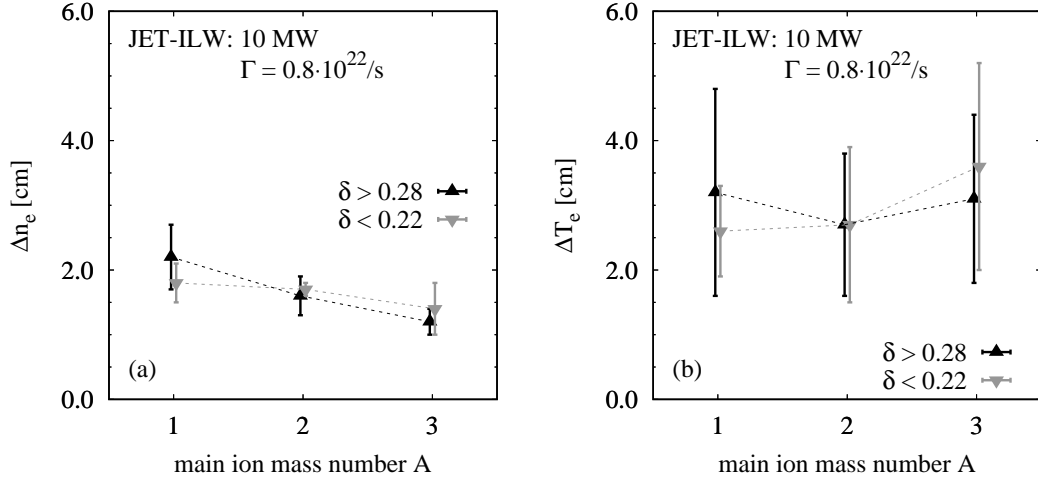


FIG. 33: Pedestal electron density (a) and electron temperature (b) widths for different main ion mass at 10 MW of heating, high  $\delta$  and low gas puff.

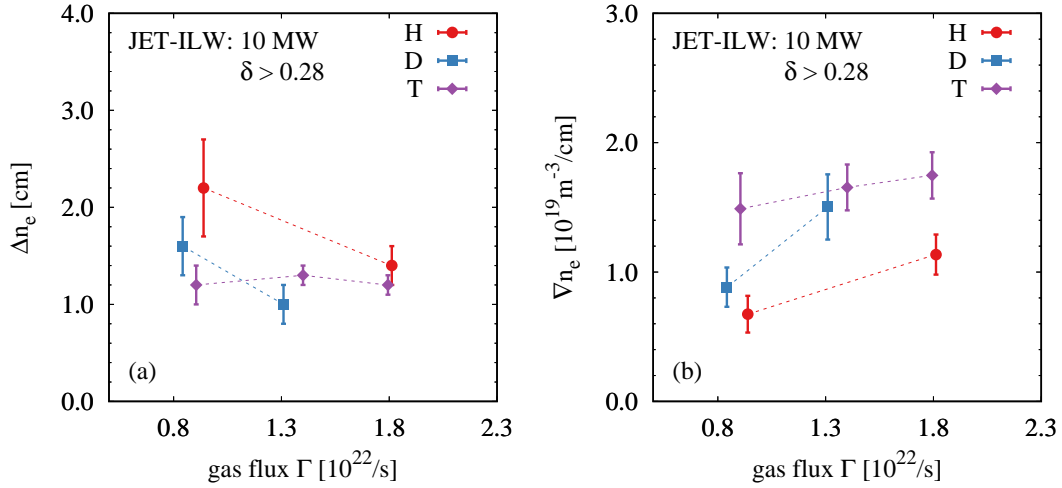


FIG. 34: Pedestal electron density width (a) and gradient (b) for different main ion masses and gas puffing at 10 MW of heating, high  $\delta$ .

gradient region and the core plasma is more gradual. In figure 33 the pedestal widths in real space coordinates are plotted against the isotope mass for low and high  $\delta$ . The density pedestal width reduces with higher mass at high  $\delta$  while it remains relatively constant at low  $\delta$ . The electron temperature pedestal width cannot be defined with the same accuracy as the density pedestal width. However, the values suggested by the bi-linear fit shown in figure 33 (b) are similar for all isotope masses which is consistent with the profiles shown in figure 32 (b). Nevertheless, they are higher than the pedestal widths determined with a modified hyperbolic tangent function, although both fitting methods are consistent within their uncertainties.

The impact of gas fuelling on the density pedestal widths and gradients is shown in figure 34. In T the pedestal width stays fairly constant while in H and D the pedestal becomes narrower with higher gas fuelling. The narrowing of the pedestal is accompanied by an increase of the density gradient which is larger than the reduction in the width. This leads to the higher pedestal top densities observed at high  $\delta$  and increasing gas puffing - also shown in figure 29. Due to the relatively constant  $\Delta n_e$  in T, a smaller increase in  $\nabla n_e$  in T, is sufficient to reach higher pedestal top densities when compared to H and D.

**ELM cycle:** To analyse the pedestal recovery after an ELM crash we investigate the H

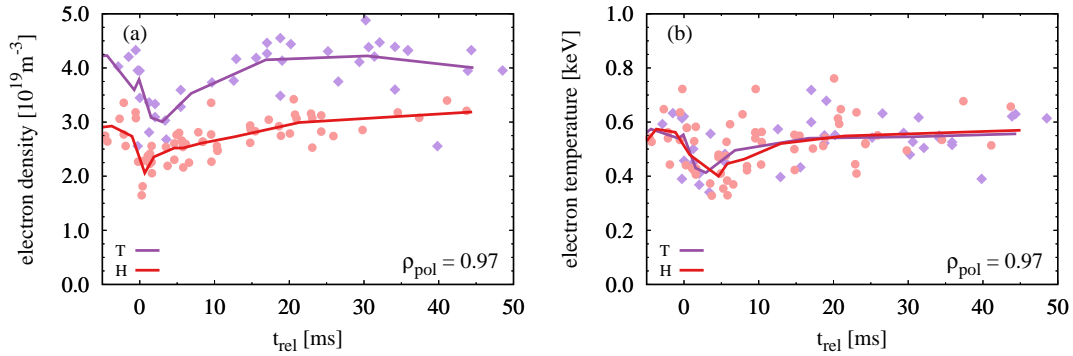


FIG. 35: Electron density (a) and temperature (b) at  $\rho_{pol} = 0.97$  after an ELM crash for different main ion masses - H: JPN97095, T: JPN98795.

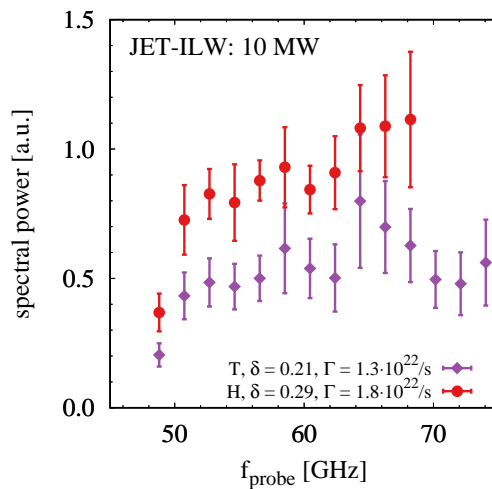


FIG. 36: Spectral power for H and T pedestals plotted against the probing frequency for a density and temperature match (cp. figure 42).

and T plasma at low gas and high  $\delta$  already shown in figure 32, where the H plasma has an  $f_{ELM}^H = 60 \pm 22$  Hz and the T plasma  $f_{ELM}^T = 32 \pm 24$  Hz. In figure 35 the recovery of the density (a) and temperature (b) pedestal at  $\rho_{pol} = 0.97$  is shown. Both H and T show data up to 50 ms after an ELM crash which is the result of the irregularity of the ELM frequency, however, the T pulse exhibits more data for longer inter ELM phases. This is due to the lower average ELM frequency. The limited temporal resolution of the Thomson scattering might obscure details of the crash, but the general trends should be recovered. The crash of the density pedestal appears to be larger in T compared to H, but the relative crash size is around 30% in both cases. The density recovers slightly faster than in T with the rate of recovery reducing after 20 ms. The temperature pedestal in H and T has a fairly similar ELM crash size and recovery characteristics as shown in figure 35 (b). The temperature at  $\rho_{pol} = 0.97$  has mostly recovered after 10 ms and only gradually increases afterwards.

**Density fluctuations:** As discussed in section 3 we use the spectral power measured by reflectometry at normal incidence as proxy for density fluctuations with low wavenumbers  $k_{\perp}$ . While this will not yield absolute fluctuation levels without appropriate full wave modelling of the diagnostic [57] the relative changes are expected to be robust. We compare plasmas with matched pedestal gradients to minimise their impact on the measured signal. The resulting spectral powers are shown in figure 36, which are clearly higher for H compared to T for the whole steep gradient region. Even if the mapping from  $f_{probe}$  to a radial location would cause a shift between the H and T data, the observation of higher spectral power in H would hold. Some of the H points at higher  $f_{probe}$  are missing, because there the Doppler shifted DBS signal starts to dominate again. This indicates that a different part of the turbulent spectrum is observed which is not comparable any more.

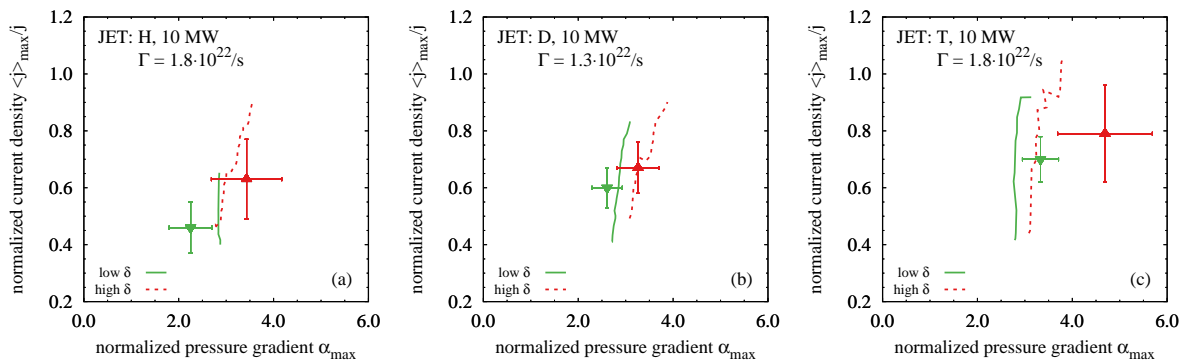


FIG. 37: Ideal peeling-ballooning stability diagrams for H (a) (JPN97094), D (b) (JPN97035) and (T) (c) (JPN100177) plasmas at high and low triangularity.

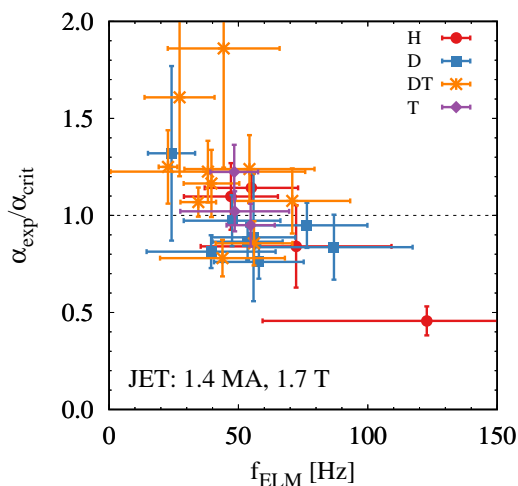


FIG. 38: Deviation of experimental pressure gradients  $\alpha_{\text{exp}}$  from peeling-ballooning stability boundary  $\alpha_{\text{crit}}$  as a function of the ELM frequency.

## 6 Pedestal stability

For the peeling-ballooning (PB) ELM stability analysis we use the ELITE [58] code. Due to the lack of highly resolved ion temperatures in the pedestal  $T_i = T_e$  is assumed. While this is the best assumption possible and at the pedestal top  $T_i \sim T_e$  is fulfilled, it could introduce systematic uncertainties if  $\nabla T_i$  is significantly different from  $\nabla T_e$ , which has been observed before in AUG [59] or DIII-D [42]. However, tests performed with  $T_i \neq T_e$  showed a negligible impact on the results compared to the  $T_i = T_e$  assumption [60]. The ideal peeling-ballooning growth rates scale with the main ion mass, but are normalized to the Alfvén frequency  $\omega_A$ . Therefore, when using a criticality condition of  $\omega_A > 0.03$  to determine the stability, the mass dependence should cancel out. This was investigated in detail for H and D [14], with the result that only a very small mass dependence is expected from ideal peeling-ballooning theory. However, this mass dependence was far from sufficient to explain the observations. A similar picture is found in our data set. In figure 37, for each isotope mass, both low and high  $\delta$  cases are compared to the PB analysis based on the experimental profiles. The small variation of the stability boundary with triangularity is an indication that the pedestals discussed here are at the ballooning boundary, because, the impact to the peeling-ballooning boundary is expected to be stronger. The stability boundaries are consistently around  $\alpha_{\text{crit}} \sim 3$  regardless of the isotope mass. The D plasmas are found exceptionally close to the predicted boundary. The low  $\delta$  H pedestal is found more in the stable region while both low and high  $\delta$  T pedestals are found to be unstable. To illustrate the general quality of the PB predictions we quantify the quality with  $\alpha_{\text{exp}}/\alpha_{\text{crit}}$  as described in [61]. The result is shown in figure 38 where a spread of  $\alpha_{\text{exp}}/\alpha_{\text{crit}}$  by over

a factor of 3 is observed. Additionally, there is no clear separation by isotope masses. This indicates that the isotope mass is unlikely to be the only reason for these differences. However, the weighting is still towards higher masses tending to be expected unstable, while the pedestal with lower masses should be more stable.

## 7 Discussion of pedestal properties

A major difficulty in describing the pedestal physics stems from the highly dynamical nature of this plasma region in the presence of ELMs. In such a situation the pedestal is not necessarily in transport equilibrium. However, for the lack of a complete model it is often assumed that before an ELM crash the plasma will be quasi stationary which then allows us to determine transport coefficients which can be compared under different conditions. Unfortunately, in H-mode ELMs exist which impose limits to the pedestal profiles which are intrinsically independent of the transport properties. To be able to discuss the relevance of our observations and what they teach us about the physics mechanisms underlying the pedestal we introduced a dynamic ELM cycle model in section 4.1. The model uses an imposed ELM stability limit and simulates the ELM recovery based on a critical gradient transport suppressed by  $\gamma_{E \times B}$  shearing. The model has no predictive capability but includes enough physics to help understanding the interactions that might govern the pedestal. The competing mechanisms are the transport which is characterised by the maximum pressure gradient that can be achieved in transport equilibrium  $\alpha_{\text{eq}}$  - when ELMs are switched off - and the critical pressure gradient  $\alpha_{\text{crit}}$  which triggers an ELM crash and is imposed arbitrarily. In the model for a fixed  $\alpha_{\text{crit}}$  with  $\alpha_{\text{crit}} < \alpha_{\text{eq}}$  the transport properties are irrelevant in determining the pedestal pressure, but the ELM frequency is strongly dependent on  $\alpha_{\text{crit}}/\alpha_{\text{eq}}$ . The farther apart are  $\alpha_{\text{crit}}$  and  $\alpha_{\text{eq}}$ , the larger is  $f_{\text{ELM}}$ . With increasing sources - heat or particles - the achievable  $\alpha_{\text{eq}}$  increases due to the self stabilisation of transport via  $\gamma_{E \times B}$ , and if  $\alpha_{\text{crit}}$  does not rise in a similar fashion, the ELM frequency increases, which is a basic property of type-I ELMs [14,62]. Experimentally we observe a strong correlation between the pedestal confinement time and the ELM frequency,  $\tau_{\text{E,ped}}$  reduces with increasing  $f_{\text{ELM}}$ . In the picture of our model a higher  $f_{\text{ELM}}$  means the ELM stability causes a larger gap between the unperturbed transport equilibrium and the ELM limited  $\alpha_{\text{crit}}$ . Therefore, naturally one could expect a lower pedestal top for higher  $f_{\text{ELM}}$ . Note that the ELM energy losses are simulated in this model but they do not have an impact on the pedestal top values. We find that the ELM energy losses in the model scale inversely proportional to the ELM frequency. Both of these model characteristics are consistent with experimental studies on ELM power losses with different isotopes [10,14].

In our ELM cycle model one route via which the isotope mass enters is the neutral penetration. For constant neutral sources and no additional mass dependence on transport this would mean in transport equilibrium we get higher densities for lower masses. This is due to larger mean free paths of the lighter neutrals and therefore a higher fuelling efficiency. However, with the existence of ELMs we are not in transport equilibrium. In fact, if there is no mass dependence introduced via stability, the higher  $\alpha_{\text{eq}}$  - due to improved fuelling efficiency at lower mass - would just result in larger  $f_{\text{ELM}}$ . For lower mass  $f_{\text{ELM}}$  is often observed to be higher [14]. Although, this is nicely consistent, on its own it is not a very strong argument.

A key assumption that we used in previous arguments [14,15,63] to highlight the importance of inter ELM transport in setting the pedestal was that with the same gas puffing and similar SOL densities we expect similar particle flow rates. Consequently, a mass dependence in the transport is required to explain the higher densities observed for higher main ion mass, despite the lower fuelling efficiency due to the shorter mean free path. However, with the new data we acquired in particular at high  $\delta$ , we have evidence that this assumption might not be accurate. In our transport model it is straight forward to introduce a mass dependence which gives a reversal of the density in the transport limited case, just as observed in experiment. This also yields a higher pedestal pressure for higher mass and otherwise constant parameters. However, the pedestal widens with increasing pressure. Additionally, when activating the ELM crash model we now get higher  $f_{\text{ELM}}$  for higher mass, because, we reduced  $\alpha_{\text{crit}}/\alpha_{\text{eq}}$ . Experimentally, we actually observe a narrowing and steepening

of the pedestal density with increasing mass and similar SOL densities. This change of pedestal width is significantly outside of the uncertainties at high  $\delta$  when comparing H and T. At low  $\delta$  and between H and D this change is less pronounced. This narrowing of the pedestal with higher density is a typical feature for a neutral penetration based pedestal width model [64], however, most reported data sets do not follow this trend [46, 65–68]. In our pedestal model with neutral penetration the narrowing of the pedestal is caused by an improvement of the fuelling efficiency. Note our definition of fuelling efficiency was an increase of particle source without changing  $n_{\text{sep}}$ . The latter is important because a higher  $n_{\text{sep}}$  tends to reduce  $\gamma_{E \times B}$  and therefore, increases transport. So in the model the experimentally observed impact is not expected to be achievable with increasing the gas puffing. Then the recycling particle flux remains a potential explanation, if this increases with isotope mass it would alter the effective particle sources in the pedestal. While the reflectivity of hydrogen isotopes on tungsten surfaces indeed increases with mass [69], this effect is relatively small and detailed neutral modelling is required to assess its relevance. Nevertheless, the impact on the density profile is more pronounced at higher triangularity where the wall clearance is reduced. Correlated with this change in wall clearance we observe a reduction of the particle flows towards the inner divertor. This could have an affect on the recycling fluxes back to the main plasma. Recent SOLPS-ITER simulations for D-T plasmas suggest that higher mass might be favorable in the distribution of neutrals in the divertor [70]. This is attributed to changing effective diffusion of neutrals with different masses when the diffusion is dominated by charge-exchange processes.

Still these mechanisms are not sufficient to explain the observed experimental profiles with different isotope masses. We require a change in the pedestal pressure with main ion mass which is only achieved by a mass dependence in the ELM stability or  $\alpha_{\text{crit}}$ . While the ideal modelling we showed in section 6 does not support such a mass dependence, this model clearly fails to capture the experimental observations. However, stability modelling taking also the resistivity into account does yield a mass dependence in  $\alpha_{\text{crit}}$  [60, 71]. Such a resistivity based model could be the basis for explaining the enhanced impact of the main ion mass at high gas fuelling rates. Nevertheless, a mass dependent  $\alpha_{\text{crit}}$  alone is also not sufficient to explain the observed profile differences. If the heat and particle transport in the pedestal are coupled - i.e. driven by an instability which affects both heat and particles - then a change in  $\alpha_{\text{crit}}$  should affect density and temperature in a similar fashion. This is for example observed for triangularity changes in H. However, the density increases with main ion mass at constant temperature. Differences in the fuelling efficiency or neutral source with main ion mass could explain this. Alternatively, one would need different mass dependencies in the heat and particle transport. In nonlinear GENE simulations exactly such mass dependencies were reported [26], in the heat transport channel the mass dependencies of turbulent ITG and neoclassical transport cancel each other, while in the particle transport the ITG mass dependence remains dominant. If instead heat and particle transport have the same mass dependence, this does not impact the pre-ELM pedestal top values if the pedestal is stability limited. In such a case we cannot deduce a mass dependence in the pedestal transport experimentally from pre-ELM measurements alone. However, if a dynamic predictive pedestal ELM-cycle model were available, then the measurements of the ELM frequency would allow to deduce the mass dependence in the pedestal transport.

The pedestal model also yields a picture for the dynamics of the recovery after an ELM crash. The model results show similarities to the measured dynamic. The temperature recovers most of its losses much faster than the density and has a slower recovery rate afterwards. Unfortunately, the low time resolution of the measurements does not allow for a more detailed comparison.

The differences with isotope mass discussed here are also consistent with estimates of the heat and particle transport for pedestal studies at constant  $\beta_N$  at higher plasma current and magnetic field [60], which is a method independent from the one presented here but with similar conclusions. In the high performance hybrid discharges [39] the first ELM crash after the entry to H-mode happens at a significantly higher pressure in T compared to D, despite a very similar evolution of density and temperature at lower pressures. This is an experimental indicator for a mass dependence in the ELM stability limit and a stability limited pedestal.

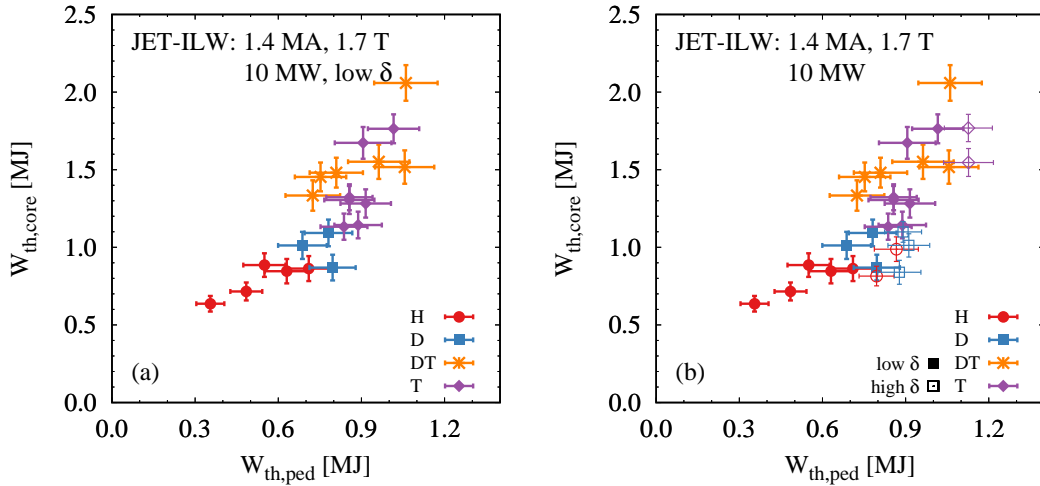


FIG. 39: Core thermal stored energy as a function of the pedestal thermal stored energy for 10 MW plasmas of a gas puffing scan for different isotopes with low  $\delta$  only in (a) and also high  $\delta$  plasmas in (b).

Although, from the profiles analysis alone we cannot quantify the mass dependence in heat and particle transport. There are observations in favour of such a mass dependent transport. The reflectometer measurements showed a significant increase of the spectral power for H compared to T which potentially corresponds to an increased density fluctuation level in the pedestal for lower main ion mass. Further observations in favour of an isotope mass dependence in the transport properties are related to L-mode [24] and L-H transitions [72–74] where the observed mass dependence cannot be explained with ELM stability. The edge transport model we discussed was able to reproduce L-H transition like behaviour, where the mass dependence in the threshold was introduced via the heat and particle transport.

## 8 Core characteristics

The impact of gas puffing and shaping on the pedestal was discussed in section 5 to better understand the physics mechanisms setting the pedestal. Now we will utilise those pedestal parameter scans to improve our understanding of the core plasma, in particular, the mass dependence of heat and particle transport.

**Medium  $\beta_N$  overview ( $\beta_N < 2.5$ ):** The majority of the data was collected at 10 MW of heating power and the gas scan at low  $\delta$  shown in figure 39 (a) highlights the strong correlation between the observed core and pedestal stored energies. A major drawback of this subset of data is that it is separated by isotope mass and due to the edge-core correlation is not sufficient for an experimental separation of mass and pedestal impact. With the additional data at high  $\delta$  this correlation is broken and as shown in figure 39 (b) we find matched pedestal pressures for different main ion masses. The DT plasmas are found with properties of the T rather than the D plasmas regarding the core and pedestal thermal energies.

**Engineering match:** The profiles for H, D and T plasmas from an engineering match are shown in figure 40. As expected from the overview plot the density increase for higher isotope mass propagates to the core, while the temperatures which are matched at the pedestal remain the same within their uncertainties and  $T_i = T_e$  for most of the radius. The rotation of the D plasma with D-NBI is the same as the one of the T plasma with T-NBI. This is expected because the higher torque input from NBI injection with heavier neutrals is mostly compensated by the larger inertia of the plasma with the higher main ion mass. The rotation in H is higher because those plasmas were heated with D-NBI and therefore have a torque input which is higher relative to the plasma inertia compared to having the same species for NBI and main ions. As expected from the matched temperature profiles no systematic isotope dependence is observed in the electron and ion heat diffusivities shown in figure 41. We find  $\chi_i \sim 2\chi_e$  for most of the radius. Note that close to edge the  $\chi_i$  values are

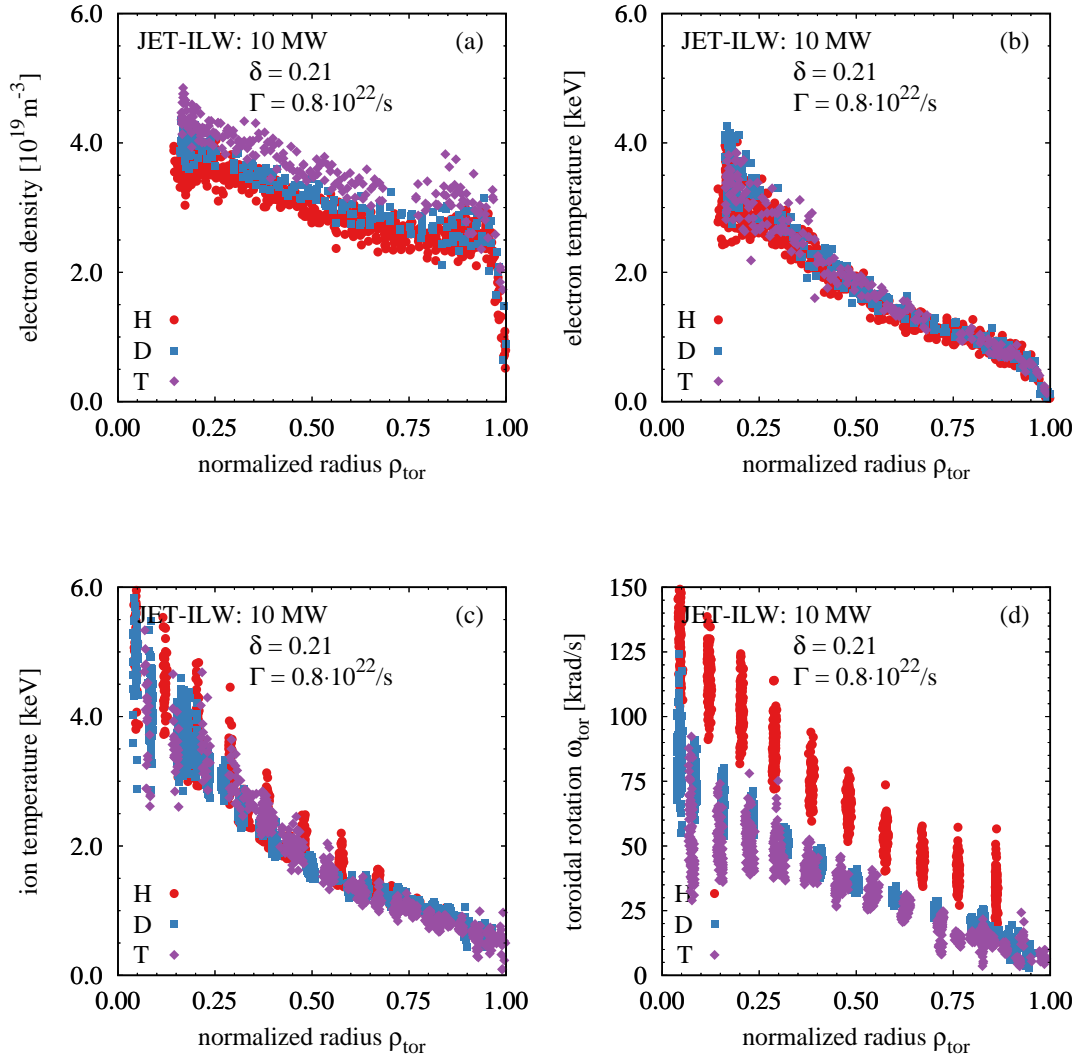


FIG. 40: Profiles of electron density (a), electron temperature (b), ion temperature (c) and toroidal angular frequency (d) for an engineering match at 10 MW, low  $\delta$  and low gas puffing but different main ion masses. H: JPN97095, D: JPN97036, T: JPN98795.

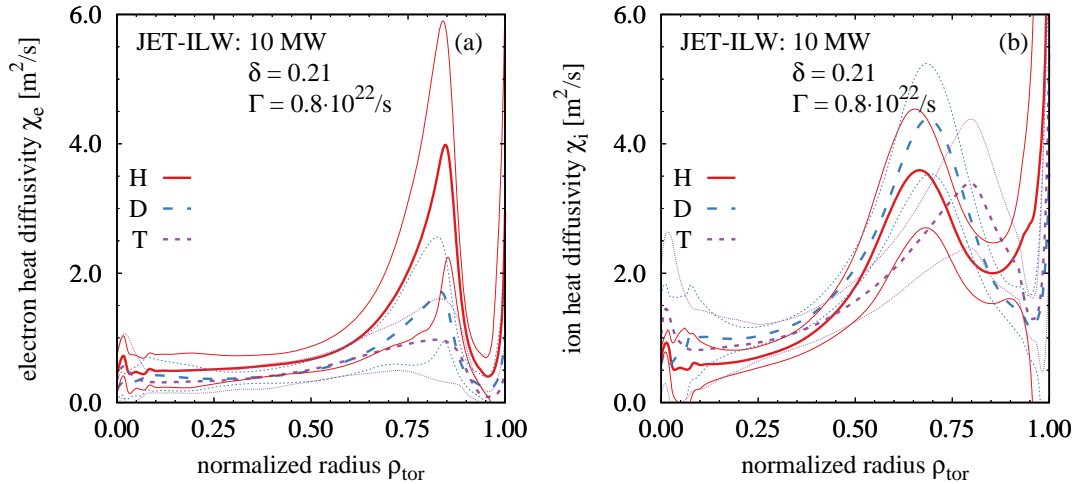


FIG. 41: Profiles of electron heat diffusivity (a) and ion heat diffusivity (b) for an engineering match at 10 MW, low  $\delta$  and low gas puffing but different main ion masses. The thin lines represent the uncertainties. H: JPN97095, D: JPN97036, T: JPN98795.

as unreliable as the uncertainties suggest because no ion temperature gradients are available for the pedestal.

**Pedestal match:** A match of the boundary at the pedestal is achieved when comparing a low  $\delta$  T plasma to high  $\delta$  H plasmas with the same heating power but different gas fuelling. The higher gas puff in H does not cause a degradation of the pedestal due to the high  $\delta$  shape as discussed in section 5. The resulting profiles are shown in figure 42 which are extremely well matched for  $n_e$ ,  $T_e$  and  $T_i$  for both isotopes with  $T_i = T_e$ , while the toroidal rotation is higher in H due to the D-NBI heating. Figure 43 shows again the electron and ion heat diffusivities this time for the pedestal match. We find  $\chi_e^H \geq \chi_e^T$ , but still similar within the uncertainties, while  $\chi_i^H = \chi_i^T$  despite the uncertainties in  $\nabla T_i$ . Again  $\chi_i$  about twice as high as  $\chi_e$ .

**High  $\beta_N$  ( $\beta_N > 2.5$ ):** Extending the data set to higher pressure is not as straight forward as for 10 MW and medium  $\beta_N$  as discussed in section 3, therefore, we have fewer comparison plasmas. This includes one T pulse (JPN99224) with  $\beta_N = 3.0$  which is compared to a D pulse (JPN97512) with matched density and  $\beta_N = 2.8$  and a D pulse (JPN96830) at lower density but matched total thermal pedestal pressure and  $\beta_N = 2.5$ . All pulses have the same NBI heating power of 13 MW with similar power density profiles but higher radiated power in T as discussed in section 2. The resulting profiles are shown in figure 44 for the density match and in figure 45 for the pressure match. At high  $\beta_N$  we find  $T_i > T_e$  for both isotope masses. The core temperature profiles for D and T have similar absolute values at mid-radius even for different densities, however, the T pulse has lower pedestal temperatures and features steeper gradients in particular for  $T_i$  and reaches higher core  $T_i$  than the D pulses. Comparing the D pulses with each other shows that the higher density also results in a higher pressure since the temperature does not drop equivalent to the density increase. Since the radiation is different for these pulses we also investigate the heat diffusivities. For the density match  $\chi_e$  and  $\chi_i$  are shown in figure 46 for D and T which are both the same over the whole radius within their uncertainties for the different isotope masses. Additionally  $\chi_e \sim \chi_i$  in the core. For the pedestal pressure match shown in figure 47 the situation is similar for  $\chi_e$  (a) which is matched between D and T, however, it is different for the ions (b) where the D pulse with lower  $n_e$  has a much higher  $\chi_i$  than the T plasma.  $\chi_i$  is most different at the outer radii of  $\rho_{\text{tor}} = 0.4 \dots 0.8$ .

**Entire database:** For the entire database the core stored energy is not a good metric because of the different heating powers which naturally give different  $W_{\text{th,core}}$ . Therefore, we are using the core energy confinement time  $\tau_{\text{th,core}} = W_{\text{th,core}}/P_{\text{sep}}$ . In figure 48 the dependence of  $\tau_{\text{th,core}}$  on the boundary condition  $W_{\text{th,ped}}$  is illustrated. For H and D plasmas there is a clear linear correlation of  $\tau_{\text{th,core}}$  and  $W_{\text{th,ped}}$  and a decent overlap for pedestal energies between 0.6 and 1.0 MJ. H plasmas extend to lower pedestal energies and D to

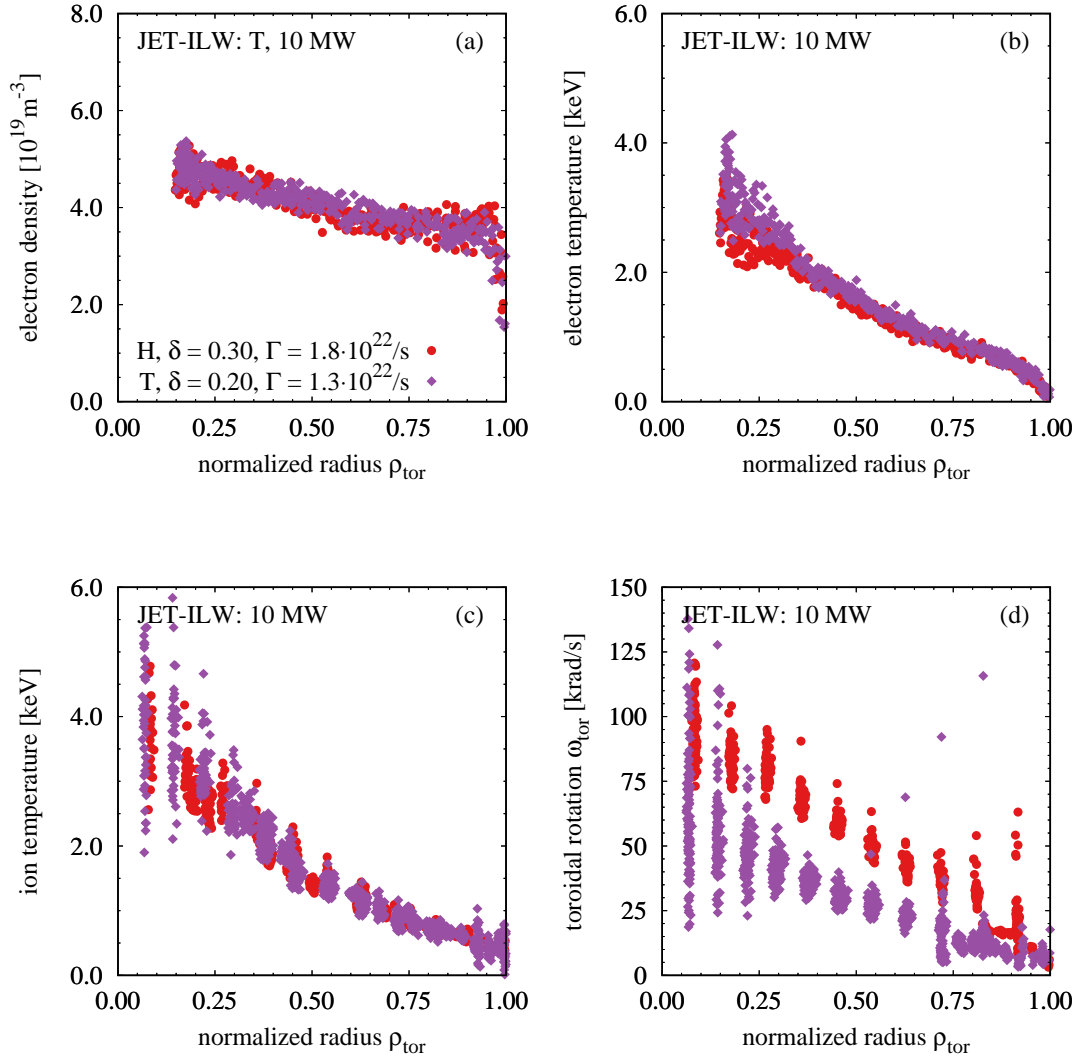


FIG. 42: Profiles of electron density (a), electron temperature (b), ion temperature (c) and toroidal angular frequency (d) for an pedestal match at 10 MW achieved with different  $\delta$  and gas puff for main ion masses H (JPN97094) and T (JPN98794).

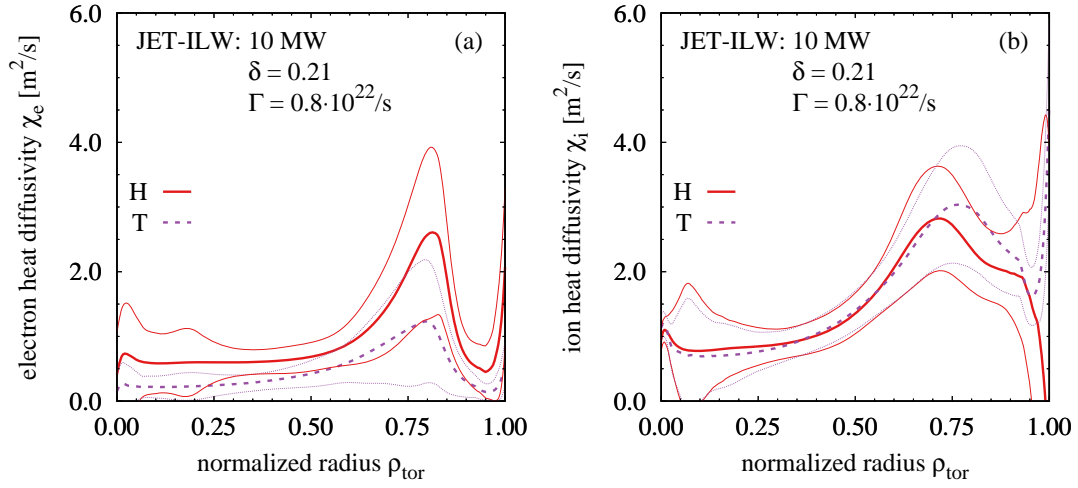


FIG. 43: Profiles of electron heat diffusivity (a) and ion heat diffusivity (b) for an pedestal match at 10 MW achieved with different  $\delta$  and gas puff for main ion masses H (JPN97094) and T (JPN98794). The thin lines represent the uncertainties.

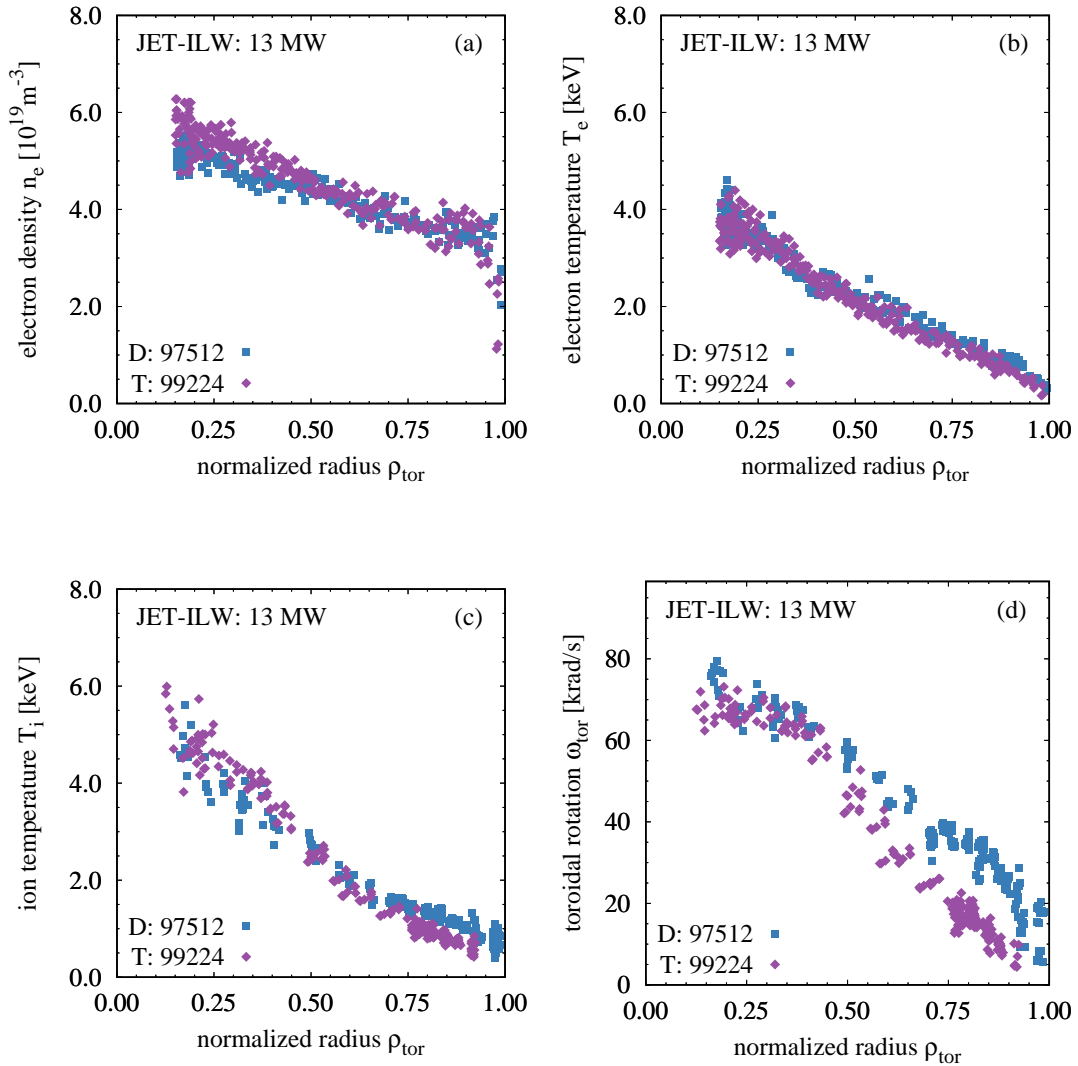


FIG. 44: Profiles of electron density (a), electron temperature (b), ion temperature (c) and toroidal angular frequency (d) for high  $\beta_N$  pulses at matched density in D (JPN97512) and T (JPN99224).

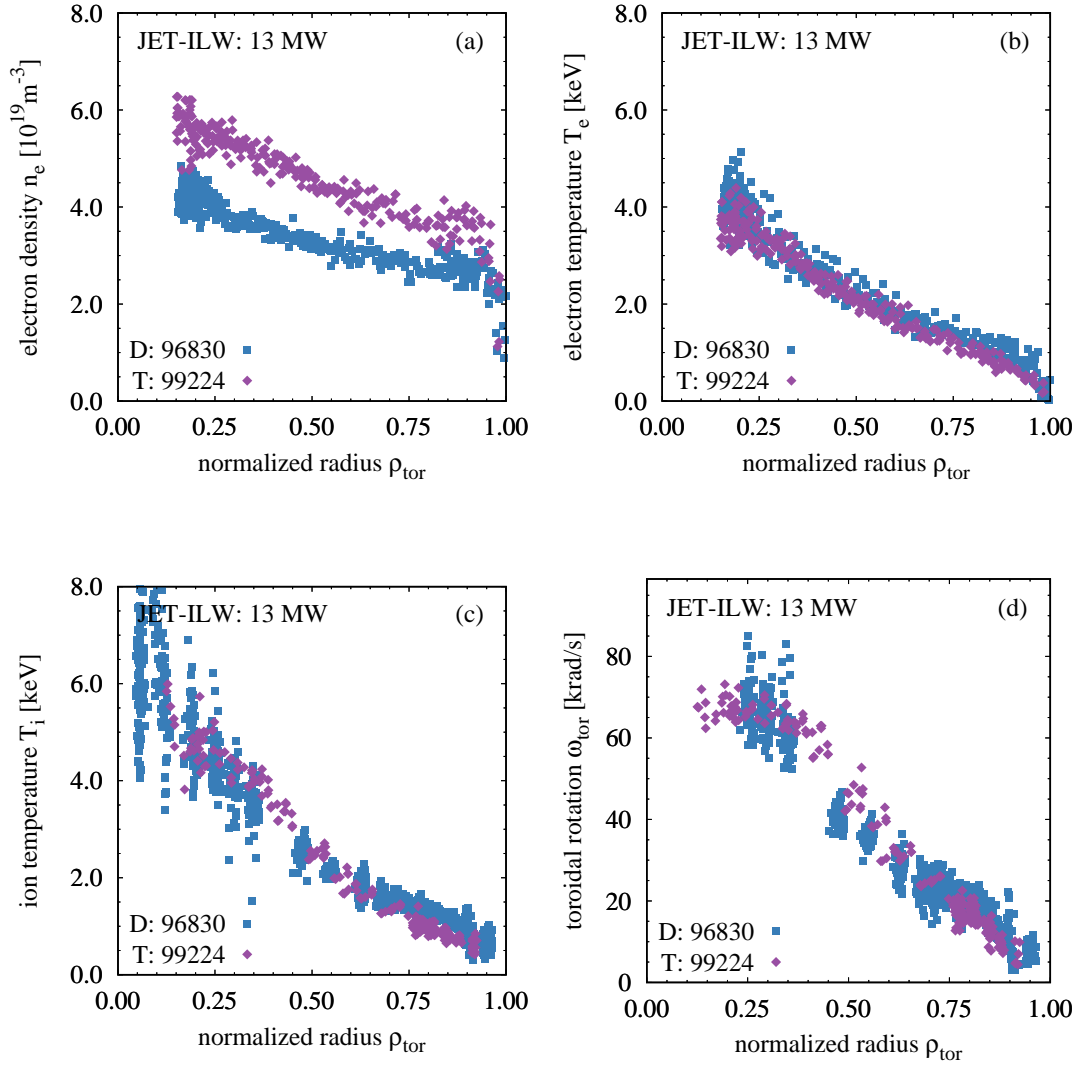


FIG. 45: Profiles of electron density (a), electron temperature (b), ion temperature (c) and toroidal angular frequency (d) for high  $\beta_N$  pulses at matched thermal pedestal pressure in D (JPN96830) and T (JPN99224).

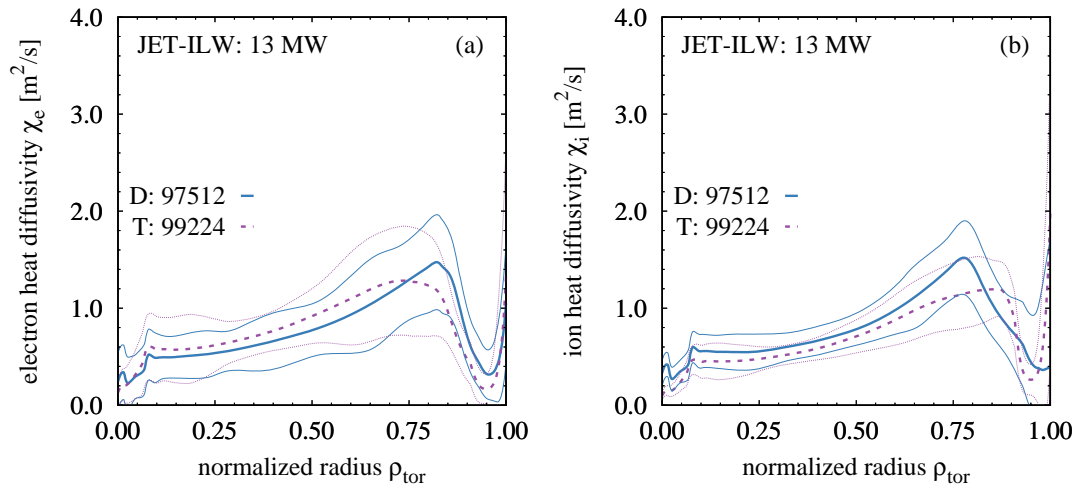


FIG. 46: Profiles of electron heat diffusivity (a) and ion heat diffusivity (b) for high  $\beta_N$  pulses at matched density in D (JPN97512) and T (JPN99224). The thin lines represent the uncertainties.

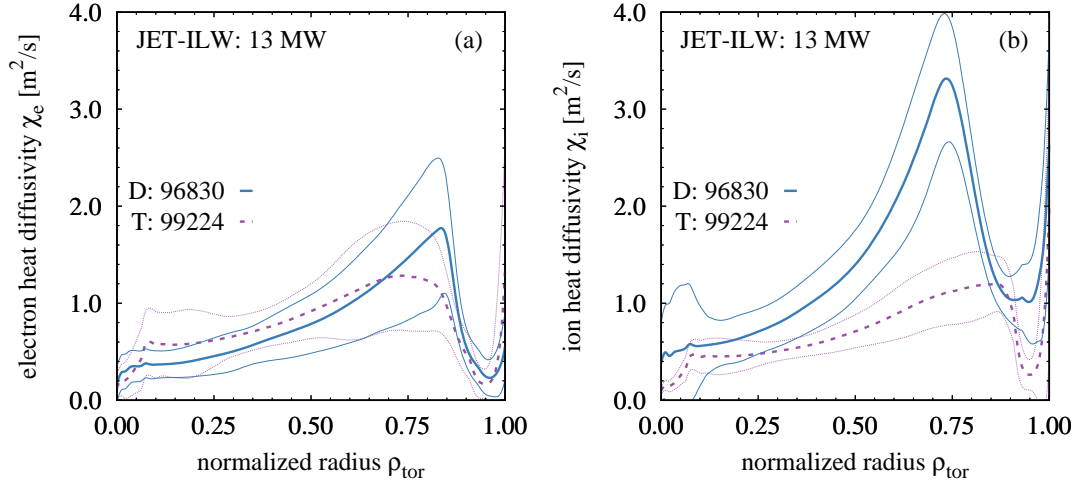


FIG. 47: Profiles of electron heat diffusivity (a) and ion heat diffusivity (b) for high  $\beta_N$  pulses at matched thermal pedestal pressure in D (JPN96830) and T (JPN99224). The thin lines represent the uncertainties.

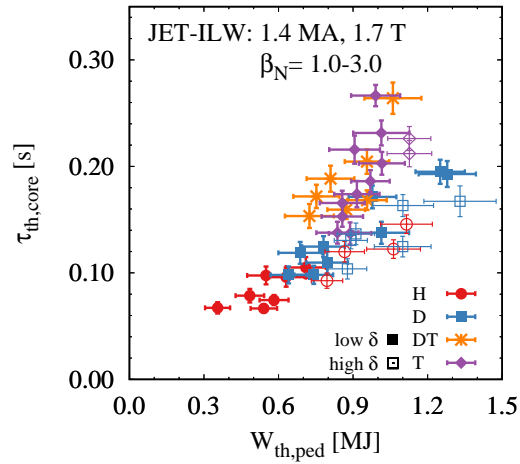


FIG. 48: Core thermal confinement time as a function of the pedestal thermal stored energy for the entire 1.4 MA, 1.7 T database.

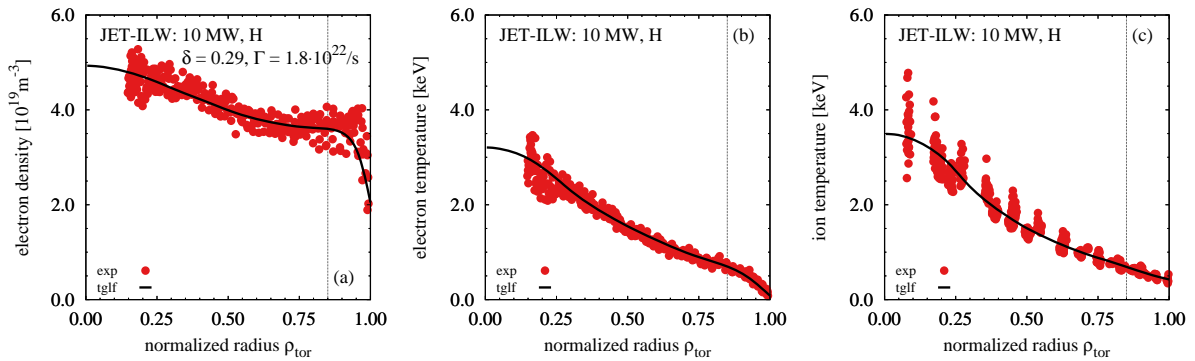


FIG. 49: Profiles of electron density (a), electron temperature (b), ion temperature (c) for the H pulse (JPN97094) of the H, T pedestal match with the experimental data as points and the prediction by TGLF-SAT2 as solid line. The position of the boundary condition for the simulation is indicated by the vertical line.

higher energies. The DT and T plasmas show a steeper slope of their  $\tau_{\text{th,core}}$ ,  $W_{\text{th,ped}}$  correlation, resulting in higher core confinement times for the same pedestal energies. Still at intermediate  $W_{\text{th,ped}} \sim 0.8$  MJ the data from all isotopes overlaps which corresponds to the profiles for the pedestal match shown above.

## 9 Core modelling

In section 4.2 we discussed known physics principles that can lead to differences in core confinement properties based on changes of isotope mass and/or pedestal properties. In this section we will quantify the theoretical expected contributions to assess where our physical understanding is lacking and to what extent our existing models are adequate to describe the observations.

### 9.1 ASTRA/TGLF-SAT2

The core transport is simulated in flux driven simulations in the ASTRA transport code [75, 76] utilizing the transport model TGLF-SAT2 [27]. We simulate  $n_e$ ,  $T_e$  and  $T_i$  while  $\omega_{\text{tor}}$  is fixed with its experimental profile. The boundary condition for the simulated quantities is also taken from experiment and fixed for  $\rho_{\text{tor}} > 0.85$ . The auxiliary heat source profiles are taken from PENCIL [77] and PION [78] and cross checked against NUBEAM while the ohmic and equipartition powers are calculated by ASTRA. For the particle sources only the neutral beam fuelling is taken into account while gas puffing and recycling sources are assumed to be covered by the experimental boundary condition. The measured radiative power is distributed over the radius assuming a flat impurity density profile. This is not necessarily true, but we lack radially resolved impurity density measurements. Fast ions are treated as non resonant species which effectively reduces the thermal ion density.

**Pedestal match:** For the pedestal match at medium  $\beta_N$  discussed in section 8 the TGLF-SAT2 predictions match the experimental core profiles extremely well. This is observed for H as shown in figure 49 as well as for T as shown in figure 50. The density peaking and  $\chi_i \sim 2\chi_e$  as well as the difference in electron and ion temperature peaking observed for both isotope masses are reproduced by the model.

**High  $\beta_N$ :** For the plasmas at higher  $\beta_N$  the core profile prediction by TGLF-SAT2 is worse than at medium  $\beta_N$ , however, not completely off. Again the observations are fairly consistent for all main ion masses and also for all transport channels. TGLF-SAT2 predicts too high transport so the resulting density and temperatures are lower than experimentally observed. In the profile comparison shown in figure 51 for D and figure 52 for T it is evident that this difference already exists for  $\rho_{\text{tor}} > 0.5$ . Interestingly, the TGLF-SAT2 heat diffusivities have  $\chi_i > \chi_e$  as in the medium  $\beta_N$  cases while the high  $\beta_N$  experimental heat diffusivities were similar for the electron and ion channel with  $\chi_i \sim \chi_e$ .

**Entire database:** We ran predictive ASTRA/TGLF-SAT2 simulations for all time slices selected for analysis. To compare with the experiment we calculate  $W_{\text{th,core}}^{(\text{TGLF})}$  and  $\tau_{\text{th,core}}^{(\text{TGLF})}$  using the predicted pressure profiles and plot the latter against the experimental boundary

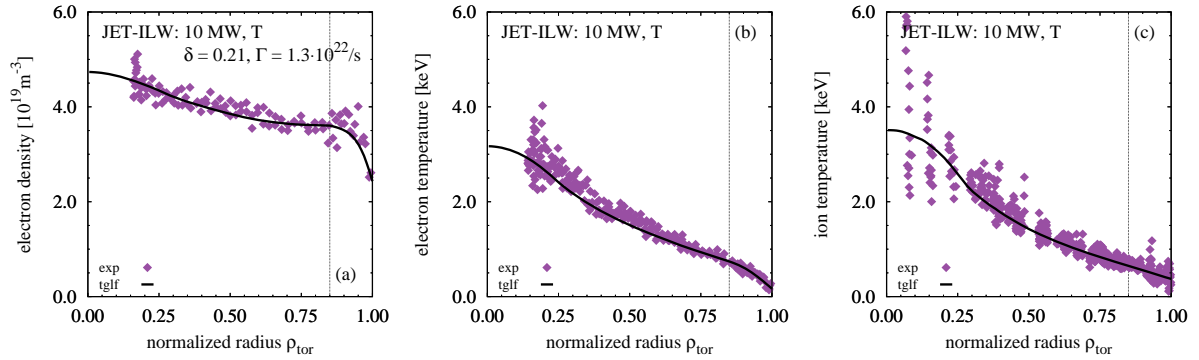


FIG. 50: Profiles of electron density (a), electron temperature (b), ion temperature (c) for the T pulse (JPN98794) of the H, T pedestal match with the experimental data as points and the prediction by TGLF-SAT2 as solid line. The position of the boundary condition for the simulation is indicated by the vertical line.

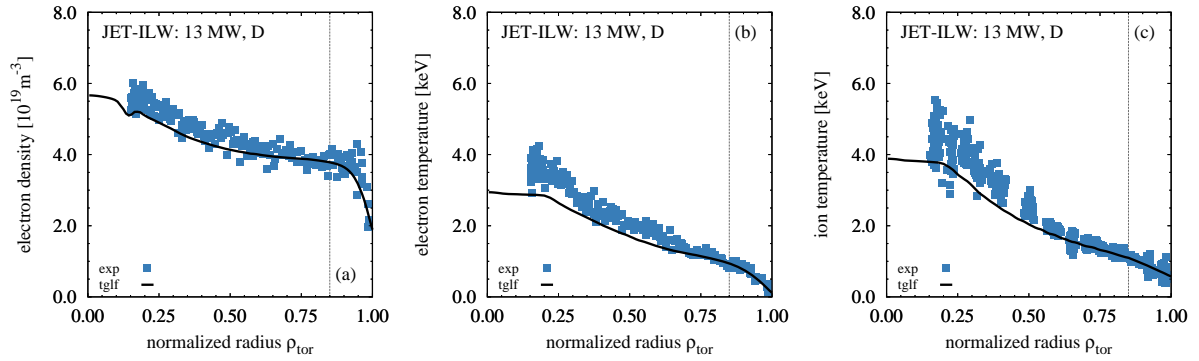


FIG. 51: Profiles of electron density (a), electron temperature (b), ion temperature (c) for the D pulse (JPN97512) of the D, T high  $\beta_N$  pedestal density match with the experimental data as points and the prediction by TGLF-SAT2 as solid line. The position of the boundary condition for the simulation is indicated by the vertical line.

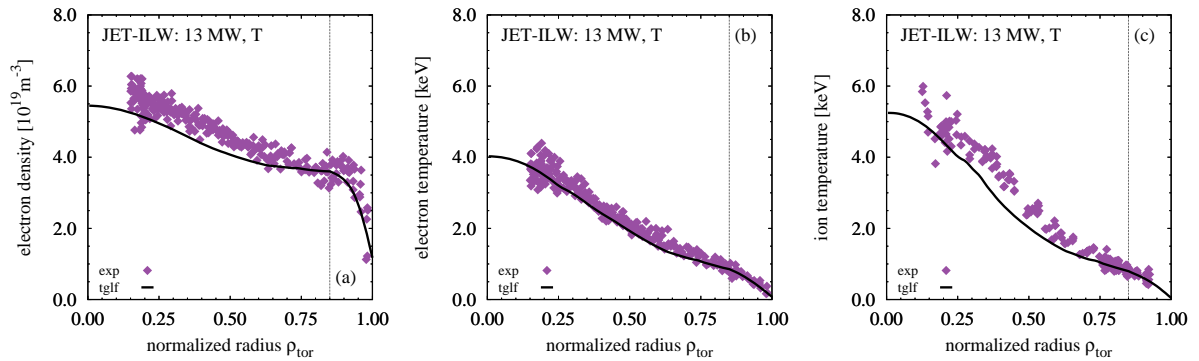


FIG. 52: Profiles of electron density (a), electron temperature (b), ion temperature (c) for the high  $\beta_N$  T pulse (JPN99224) with the experimental data as points and the prediction by TGLF-SAT2 as solid line. The position of the boundary condition for the simulation is indicated by the vertical line.

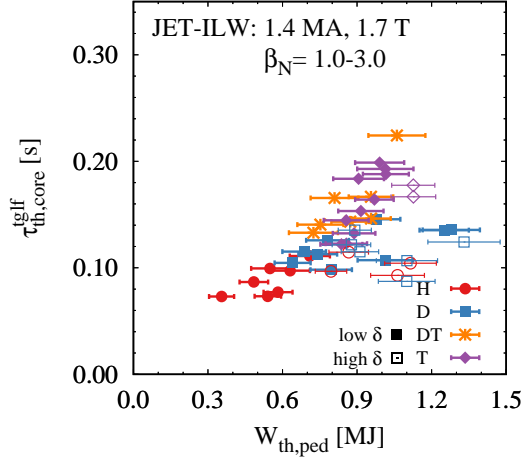


FIG. 53: TGLF-SAT2 prediction for the core thermal confinement time as a function of the pedestal thermal stored energy for the entire 1.4 MA, 1.7 T database.

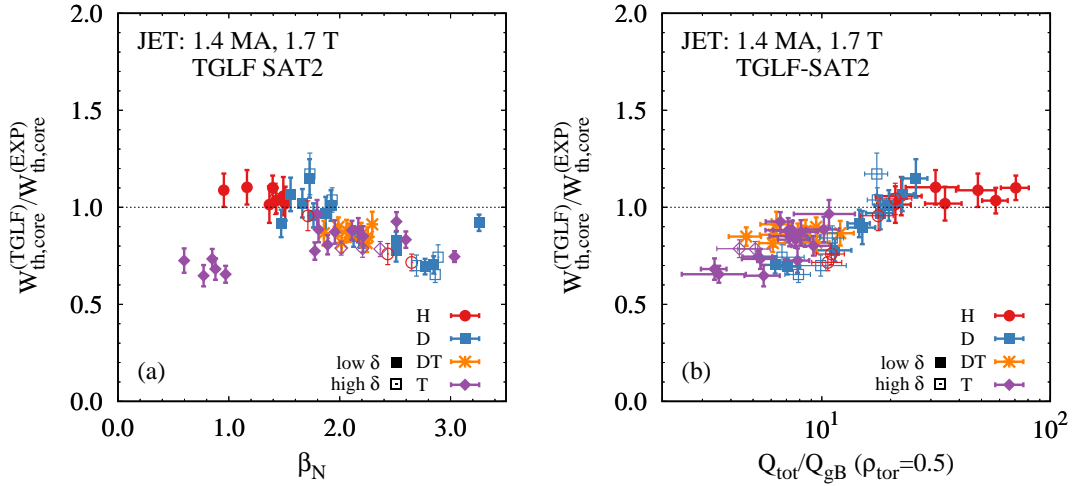


FIG. 54: Quality of the TGLF-SAT2 predictions for the core thermal energy as a function of the normalized pressure  $\beta_N$  (a) and the heat flux in gyroBohm units at mid radius (b).

condition. The result is shown in figure 53 and should be compared to its counterpart based on experimental core data shown in figure 48. From this comparison it becomes evident that TGLF-SAT2 is able to reproduce two key features observed experimentally, the correlation between the core confinement time and the pedestal pressure, as well as the separation of DT and T plasmas from their H and D counterparts at high pedestal pressures. Despite these agreements also systematic deviations are showing, in particular, at higher  $W_{th,ped}$  in the form of a discontinuity in the experimentally linear trend of H and D data. Note this is the same overestimation of transport already shown for the individual high  $\beta_N$  profiles.

For further investigation of this discrepancy we utilize the deviation of predicted and observed core energies  $W_{th,core}^{(TGLF)}/W_{th,core}^{(EXP)}$ . We find a strong correlation between  $W_{th,core}^{(TGLF)}/W_{th,core}^{(EXP)}$  and the normalized total pressure  $\beta_N$  as well as the heat flux in gyroBohm units  $Q_{tot}/Q_{gB}$  at  $\rho_{tor} = 0.5$  as shown in figure 54. TGLF-SAT2 overestimates the transport at high  $\beta_N$  or low  $Q_{tot}/Q_{gB}$ , where the latter corresponds to a closeness to the turbulent threshold. To gain additional insight regarding both correlations we added data with  $\beta_N < 1.0$  and very low  $Q_{tot}$  just for this comparison. These plasmas are at  $P_{heat} \sim 3 \dots 5$  MW which is closer to the L-H power threshold than the bulk of the higher  $\beta_N$  pulses with  $P_{heat} \geq 10$  MW. TGLF-SAT2 also overestimates transport for these plasmas, thereby, breaking the  $\beta_N$  correlation, while being consistent with the  $Q_{tot}/Q_{gB}$  one.

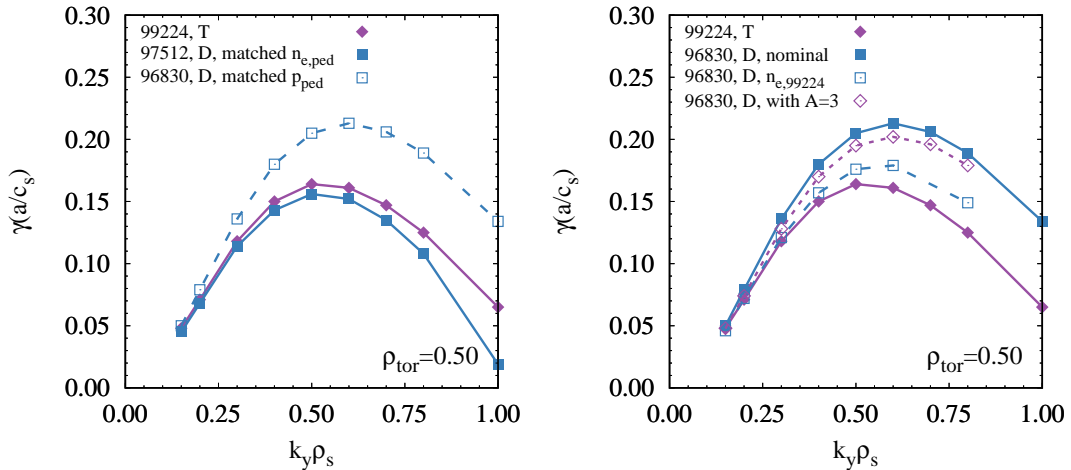


FIG. 55: Nominal linear growth rates for the D density and pressure match with T at high  $\beta_N$  (a). Growth rates for pressure match with main ion mass and density variations. The sound speed  $c_s$  in the normalisation is calculated with corresponding main ion mass.

## 9.2 GENE modelling

To better understand the potential physics processes dominating the plasmas discussed here we perform gyrokinetic simulations. In this section we present the results of local linear and nonlinear gyrokinetic simulations with the GENE code [79]. GENE solves the gyro-kinetic Vlasov equations [80,81] which are coupled with the Maxwell equations within a  $\delta f$  approximation. It uses a set of field aligned coordinates  $\{x, y, z, v_{\parallel}, \mu\}$  where  $z$  is the coordinate along the magnetic field line,  $x$  is the radial and  $y$  is the binormal one,  $v_{\parallel}$  is the parallel velocity and  $\mu$  is the magnetic momentum. The simulations are carried out in the local limit using realistic geometry as discussed in section 3, collisions enter via a Landau-Boltzmann operator, finite- $\beta$  effects are considered with both  $B_{\perp}$  and  $B_{\parallel}$  fluctuations, kinetic ions and electrons use the realistic mass ratio. External flow shear  $\gamma_{E \times B}$  effects are only considered for selected simulations. Fast ions are not considered as the fast-ion pressure profiles are relatively similar as discussed in section 2. No impurities have been considered in the simulations since the experimental values of  $Z_{\text{eff}}$  for these pulse are low ( $Z_{\text{eff}} < 1.5$ ). Typical grid parameters in the non-linear simulations were as follows: perpendicular box sizes  $[L_x, L_y] \approx [190, 200]\rho_s$ , phase-space grid discretization  $[n_x, n_y, n_z, n_{v_{\parallel}}, n_{\mu}] \approx [384, 64, 40, 48, 16]$  and  $0.15 \lesssim k_y \rho_s \lesssim 1.00$ . In all the simulations, the nonlinear fluxes are mainly related to the electrostatic potential  $\phi$  fluctuations while the contribution from the parallel magnetic potential  $A_{\parallel}$  fluctuations are smaller ( $\sim 5\%$  of the total fluxes). We focus the investigations on the high  $\beta_N$  discharges where TGLF-SAT2 overestimated the transport as discussed in section 9.1.

**Linear GENE modelling:** Close to the plasma center at  $\rho_{\text{tor}} = 0.3$  we find these high  $\beta_N$  plasmas linearly stable against instabilities, this is due to strong EM stabilisation. When we investigate at mid radius  $\rho_{\text{tor}} = 0.5$  ion temperature gradient ITG turbulence becomes dominant. The normalized growth rates  $\gamma(a/c_s)$  for one T and two D plasmas are shown in figure 55 (a), the T and D plasmas with matched pedestal density have very similar  $\gamma(a/c_s)$  while the D plasma with the pedestal pressure match - at lower density - is found with a 30% higher growth rate. The main driver of this difference is the density. In figure 55 (b) growth rates from different simulations are shown for the pressure matched D plasma, one in its nominal form, one with the main ion isotope mass changed to T and one with the density of the T plasma. Changing to a higher isotope mass slightly reduces the growth rates (5%) and thereby weakening the gyroBohm mass scaling from the normalisation. Increasing the density has a more significant impact on the growth rates (20%).

**Non-linear GENE modelling:** The strong impact of the EM stabilisation is also observed nonlinearly, as shown in figure 56, with a  $\beta_e$  of  $\sim 2\%$  the modelled heat fluxes are close to 0 for D and T. This is the case even without  $\gamma_{E \times B}$  effects being considered, which normally would have an additional stabilising effect. The two T plasmas with the very different

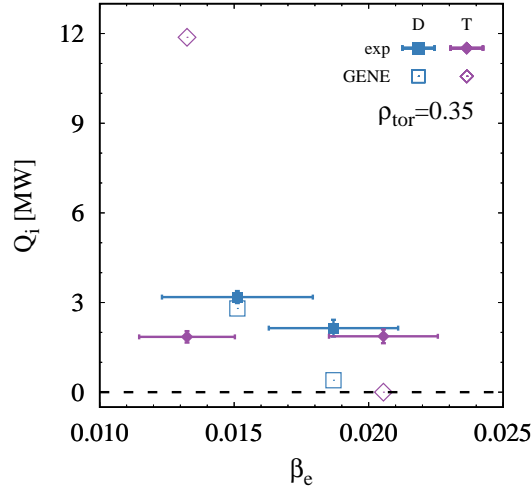


FIG. 56: Nonlinear ion heat fluxes plotted against  $\beta_e$  with solid symbols for experimental and open for GENE values.

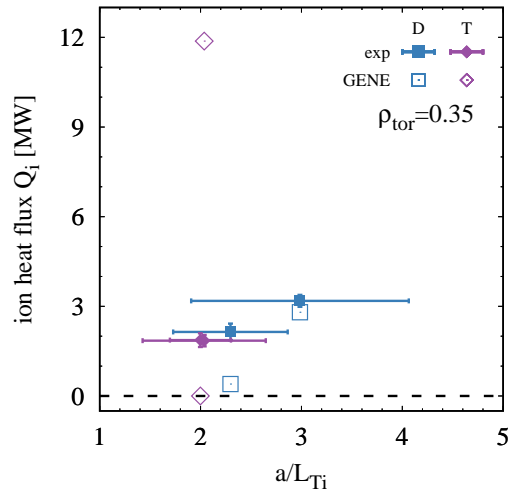


FIG. 57: Nonlinear ion heat fluxes plotted against the normalized inverse ion temperature gradient length with solid symbols for experimental and open for GENE values.

heat fluxes actually have the same ion temperature gradient lengths  $a/L_{Ti}$  highlighting the importance of EM stabilisation in these simulations. This is shown in figure 57 where the two experimental points lie on top of each other, when plotted against  $a/L_{Ti}$ . In this plot we also see the expected trend with the turbulent drive  $a/L_{Ti}$ . Indeed when  $a/L_{Ti}$  is increased for the high  $\beta_e$  T case up to the limit of experimental uncertainties the modelled heat fluxes are found at more realistic values. However, including  $\gamma_{E \times B}$  effects again results in a complete stabilisation of the turbulence and close to zero heat fluxes. Without  $\gamma_{E \times B}$  effects active the modelled heat fluxes are found to follow the gyroBohm scaling when varying the mass number.

Unfortunately, the simulations performed for this publication remain inconclusive with respect to the isotope mass. This is because we did not achieve a case with realistic heat fluxes, while having the physics active which can potentially introduce a mass dependence. The sensitivity studies expected to be necessary for a robust conclusion would require variations in  $\beta_e$ ,  $a/L_{Ti}$ ,  $\omega_{tor}$ , radius and simulation domain size which would go beyond the scope of this publication. Such a study will have to be presented in a future publication.

## 10 Discussion of core properties

Experimentally we can clearly distinguish the heat transport properties between the medium and high  $\beta_N$  type-I ELMy H-mode plasmas. At medium  $\beta_N$  we find  $T_i = T_e$  despite higher ion heating which is caused by  $\chi_i > \chi_e$ . This is accompanied by a relatively low density peaking of 1.2. This is observed similarly in H and T plasmas with matched pedestal parameters and consistent with the H and D comparisons already reported in [15]. At higher  $\beta_N$  the ion and electron heat diffusivities are more similar  $\chi_i \sim \chi_e$  over most of the radius, consequently, the higher ion heating by NBI results in  $T_i > T_e$  at the same time the density peaking increases to 1.5. This is mainly observed for high densities and then for D and T alike. At lower densities, which could not be accessed in T, D plasmas are found with  $\chi_i > \chi_e$  even at higher  $\beta_N$  and similar pedestal pressures than T plasmas at higher density. We find that DT and T plasmas can have higher core confinement time than their H and D counterparts at similar pedestal energies. Although, this could suggest an isotope mass dependence in the core transport, we can reproduce the difference quantitatively with the TGLF-SAT2 transport model. We observe deviations between TGLF-SAT2 and the experiment, which will be discussed below, however, these deviations are the same for H, D, DT and T thus we cannot infer a mass dependence for them. TGLF-SAT2 is based on a gyroBohm mass dependence and yields  $W_{th,core} \propto A^{-0.156}$  when taking the equipartition into account. This is exactly the mass dependence of core confinement as observed in type-I ELMy H-modes in the JET DTE1 campaign [8], where  $\tau_{core} \propto A^{-0.16}$  was reported.

One factor contributing to the apparent mass dependence in the core confinement is the strong impact of core-edge coupling. A higher pedestal pressure will in general result in an increased core energy due to profile stiffness. Additionally, a higher pedestal density at constant pressure and therefore a lower temperature will reduce the gyroBohm factor in the core and allow for a higher turbulent drive, i.e. temperature gradients, at constant heat fluxes in MW. This argumentation is not necessarily valid for plasmas with features which alter the core transport locally, like internal transport barriers ITBs or MHD modes. Note that the experimental edge mass dependence is an input to the core simulations with TGLF-SAT2. So it is no surprise that TGLF-SAT2 can reproduce the indirect mass dependence observed in the core so well.

So the fact that T pulses are generally found at higher pedestal densities than H and D plasmas as discussed in section 7 will directly impact the core performance as well. At high  $\beta_N$  this is confirmed by comparisons with matched and different densities. The D plasma with lower  $n$  but similar  $T_e$  and  $T_i$  has significantly higher  $\chi_i$  than its T and D counterpart at higher density. The beneficial impact observed at higher density is supported by linear GENE simulations which find lower growth rates at higher densities, while the influence of the mass number is comparably small. Unfortunately, the investigation with non-linear GENE simulations in the local approximation where inconclusive. The simulations suggest a strong impact of the EM stabilisation on the turbulent heat fluxes, which would be an additional mechanism where a high pedestal pressure might prove beneficial for core confinement as

well. However, the modelled absolute heat fluxes are so far from the experimental values that their relevance remains questionable. A sensitivity study to scan the experimental inputs within their uncertainties is required to improve the significance of the results.

The systematic deviations observed between TGLF-SAT2 and the experiment, cannot be resolved by introducing an additional mass dependence to the core transport model. A convenient explanation would be the missing EM stabilisation in TGLF-SAT2, which could be responsible for the overestimation of transport at high  $\beta_N$ . For those plasmas the GENE simulations highlighted the importance of EM stabilisation. However, we also find overestimated transport at very low  $\beta_N$ . While one could argue that these plasmas are quite different from the main database, as they have very low heating power just above the LH power threshold, there is another parameter where the deviation for low and high  $\beta_N$  aligns. This is the heat flux in gyroBohm units  $Q_{\text{tot}}/Q_{\text{gB}}$ . For low  $Q_{\text{tot}}/Q_{\text{gB}}$  the transport is overestimated by TGLF-SAT2 while its prediction is accurate for larger  $Q_{\text{tot}}/Q_{\text{gB}}$ . This does indicate that close to the threshold of turbulent transport the model cannot capture the physics any more. TGLF-SAT2 predicts  $\chi_i > \chi_e$  for plasmas with  $\chi_i \sim \chi_e$  which suggests a reason for the discrepancy could originate in the ion heat transport channel. Additionally, TGLF-SAT2 predicts a change of the density peaking with ion mass which is not observed to such an extent in our data set. The measured density peaking is fairly similar for different isotopes, but increases with plasma pressure. The medium  $\beta_N$  pulses have a density peaking of  $\sim 1.2$  which is predicted well by TGLF-SAT2, the high  $\beta_N$  pulses have a stronger density peaking of  $\sim 1.5$  while the prediction for those plasmas falls short by about 20%.

We do need to add a disclaimer to the statement regarding the absence of an isotope mass dependence on the core transport. While it is true for the type-I ELMy H-modes and the relatively wide parameter scan we investigated here, it might change when other physics mechanisms become important. One such effect which is well known is the turbulence stabilisation by fast ions and the fast-ion content often varies with isotope mass [13]. In particular, in the presence of a significant  $\alpha$  particle population it is likely not negligible. However, for the data set discussed here the fast-ion content is relatively low  $\leq 20\%$  and shows no systematic correlation with the main ion mass in the plasma. While we do expect higher fast-ion content due to T neutral beam injection, the T plasmas are found at higher densities and consequently lower temperatures which mitigates the difference due to the mass in the fast-ion slowing down.

## 11 Summary

We presented the results of a three isotope scan H, D, T in type-I ELMy H-mode with varying gas fuelling, triangularity and a power variation that resulted in normalized pressures  $\beta_N = 1.0 \dots 3.0$ . This data is complemented by D-T mixture plasmas with the same heating and only minor variations in the total gas fuelling. For this data set we investigated the pedestal characteristics and the core transport. In the analysis we focus on ways to provide restrictions to theoretical models based on our experimental findings.

In the pedestal the data shows a strong mass dependence which changes with gas fuelling. Low  $\delta$  H plasmas loose pedestal pressure with gas fuelling while not gaining in pedestal top density. D plasmas also loose pedestal pressure with gas fuelling while the pedestal top density slightly increases. Higher gas fuelling in T plasmas increases the density at constant pressure. Consequently, we observe different isotope mass scalings for the pedestal density depending on the gas fuelling level. This strongly suggests that a mass scaling is likely only valid for the parameter range it was derived on. Extrapolations or applications to different plasma scenarios need to be discussed with this in mind.

To understand the interplay of the different physics in the pedestal we developed an empirical model based on  $\gamma_{E \times B}$  turbulence mitigation and realistic neutral penetration with the option to simulate ELM cycles. In this model a higher separatrix density due to increased gas fuelling directly results in reduced pedestal pressure. However, this would be the same for all isotope masses. Therefore, differences in the fuelling efficiency with the isotope mass would be necessary to reproduce the observations of higher densities in T. With dynamic ELM cycles it becomes clear that two ingredients are required to reproduce the observations:

a mass dependence in the ELM stability and a separation of heat and particle transport which depends on the isotope mass. A mass dependence which acts equally on the heat and particle transport channel would not change the pedestal density to temperature ratio which is observed in experiment with changing mass number. Such a mass dependence in the transport would only change the ELM frequency. As observed before the higher ELM frequencies correlate with reduced confinement in our data set. Our dynamic ELM cycle modelling suggests that higher ELM frequencies might not be the cause for the reduced confinement, but the natural consequence of a more unstable pedestal. With a predictive ELM cycle model one could potentially extract crucial information out of the pedestal dynamics. This would require an integrated treatment of pedestal stability with a realistic transport model.

The core plasma scales with the pedestal. A higher pedestal pressure directly improves the core confinement of type-I ELMy H-modes. T plasmas are observed with a unique pedestal composition of high densities and only moderately reduced temperatures. A consequence is that plasmas with T can show an improved core confinement even for similar pedestal pressures as H and D plasmas. This core-edge coupling is reproduced in flux driven TGLF-SAT2 simulations, when the measured pedestal is set as the boundary condition. This means that fairly basic physics mechanisms seem to be dominating this coupling. Although, within our experimental uncertainties we cannot exclude that there might be an additional mass dependence in the heat and particle transport the modelling suggests it is not crucial to explain the observations. Note that in this context no mass dependence still means a deviation from the pure gyroBohm scaling. Given the popularity of power law scalings including the main ion mass, we want to stress that a scaling, which does not separate core and pedestal parameters and includes pedestal parameters in the scaling for the core properties, cannot be expected to yield good results when used for extrapolations.

Consistent with other studies as quoted in section 1 and those for the high performance hybrid and baseline discharges [39,82], we conclude that with varying main ion masses the differences in basic parameters such as pedestal pressure, pedestal density or fast-ion content can explain the bulk of changes in the core confinement. When minimising these differences between plasmas with varying isotope mass also the differences in core confinement reduce. Such an explanation does not work for the pedestal. To explain the observations in the pedestal, we require an explicit mass dependence in the ELM stability and different mass dependencies in heat and particle transport. The latter could be due to different properties of the dominating transport processes or due to a mass dependence in the particle sources.

The implications from this work for larger machines like ITER are the following. The buildup of the pedestal density and the particle transport and sources have significant impact on the whole plasma and change rather strongly with isotope mass. However, it is not directly clear how this translates to ITER where the SOL is expected to be opaque meaning that the divertor and pedestal plasma become decoupled which is not the case in present day devices [83,84]. In the core of the plasma we expect fewer surprises, the transport is observed without strong mass dependence when other influences are minimised. One of the state of the art transport models used for predicting future fusion devices TGLF-SAT2 does a good job to predict the isotope mass dependence of heat and particle transport. The model does this by capturing transport effects which are indirectly connected with a change of mass, but do not result from an explicit dependence of transport on the isotope mass. In our dataset these indirect effects are introduced by the boundary condition. TGLF-SAT2 over predicts the transport in the regime of low gyroBohm heat fluxes which is a regime most relevant for fusion plasmas due to their high temperatures. Lower transport in the real plasma is in general a positive observation, still it leaves some uncertainties regarding the applicability of this model in such regimes. One important difference in fusion devices will be the high fast-ion population in the form of  $\alpha$  particles, whose impact TGLF-SAT2 cannot describe at the moment. However, in our plasmas fast ions played a minor role, therefore, we cannot contribute to this question. JET H-mode plasmas with higher fusion rates and  $\alpha$  particle population are reported in [39,85]. In addition, ITER cannot have type-I ELMs, therefore, investigations of the isotope mass dependence for pedestals with no or small ELMs are required, which was not investigated here.

Experimental studies regarding isotope physics have one difficulty in common, the main

isotope is never the only quantity that is changed in the experiment. We have highlighted the importance of the coupling of transport regions which results in correlations between different parameters. Also the coupling between the transport channels can become relevant. In addition, there will be changes due to the execution of the experiment when operating with different isotope masses. This means we are typically dealing with a transport problem which is under determined given the amount of experimental freedom one has in a tokamak plasma. Therefore, the experiments including the hydrogen isotope tritium presented here are extremely useful, as they do add a new angle which helps to solve the transport problem.

*The authors thank E. Fable and G. Tardini for their support in running the ASTRA transport code. The authors thank G. Conway and C. Silva for fruitful discussions about the interpretation of the Doppler reflectometer data. This work has been carried out within the framework of the EUROfusion Consortium, funded by the European Union via the Euratom Research and Training Programme (Grant Agreement No 101052200 - EUROfusion) and from the EPSRC [grant number EP/W006839/1]. Views and opinions expressed are however those of the author(s) only and do not necessarily reflect those of the European Union or the European Commission. Neither the European Union nor the European Commission can be held responsible for them.*

- [1] BESSENRODT-WEBERPALS, M. et al., Nuclear Fusion **33** (1993) 1205.
- [2] SCHNEIDER, P. A. et al., Nuclear Fusion **57** (2017) 066003.
- [3] DELABIE, E. et al., Preliminary interpretation of the isotope effect on energy confinement in Ohmic discharges in JET-ILW, in *44th EPS Conference on Plasma Physics*, page P4.159, Geneva, 2017, European Physical Society.
- [4] KUPRIENKO, D. V. et al., Plasma Physics Reports **45** (2019) 1128.
- [5] MAGGI, C. F. et al., Nuclear Fusion **59** (2019) 076028.
- [6] CHALLIS, C. D. et al., Nuclear Fusion **55** (2015) 053031.
- [7] SAIBENE, G. et al., Nuclear Fusion **39** (1999) 1133.
- [8] CORDEY, J., Nuclear Fusion **39** (1999) 1763.
- [9] URANO, H. et al., Nuclear Fusion **53** (2013) 083003.
- [10] LAGGNER, F. M. et al., Physics of Plasmas **24** (2017) 56105.
- [11] MAGGI, C. F. et al., Plasma Physics and Controlled Fusion **60** (2018) 14045.
- [12] WEISEN, H. et al., Journal of Plasma Physics **86** (2020) 905860501.
- [13] SCHNEIDER, P. A. et al., Nuclear Fusion **61** (2021) 036033.
- [14] HORVATH, L. et al., Nuclear Fusion **61** (2021) 046015.
- [15] SCHNEIDER, P. A. et al., Nuclear Fusion **62** (2022) 26014.
- [16] GARBET, X. et al., Plasma Physics and Controlled Fusion **46** (2004) 1351.
- [17] CAMENEN, Y. et al., Nuclear Fusion **47** (2007) 510.
- [18] SCOTT, S. D. et al., Physics of Plasmas **2** (1995) 2299.
- [19] BONANOMI, N. et al., Nuclear Fusion **59** (2019) 096030.
- [20] WALTZ, R. E. et al., Physical Review Letters **65** (1990) 2390.
- [21] GARCIA, J. et al., Plasma Physics and Controlled Fusion **64** (2022) 54001.
- [22] GARCIA, J. et al., Nuclear Fusion **57** (2017) 014007.
- [23] BUSTOS, A. et al., Physics of Plasmas **22** (2015) 012305.
- [24] BONANOMI, N. et al., Nuclear Fusion **59** (2019) 126025.
- [25] BELL, E. A. et al., Physics of Plasmas **26** (2019) 82305.
- [26] PREDEBON, I. et al., Nuclear Fusion **63** (2023) 36010.
- [27] STAEBLER, G. M. et al., Nuclear Fusion **61** (2021) 116007.
- [28] CANDY, J. et al., Journal of Computational Physics **324** (2016) 73.
- [29] DUDDING, H. G. et al., Nuclear Fusion **62** (2022) 96005.
- [30] LUDA, T. et al., Plasma Physics and Controlled Fusion **65** (2023) 34001.
- [31] JOFFRIN, E. et al., Nuclear Fusion **45** (2005) 626.
- [32] MAGGI, C. F., Nuclear Fusion **47** (2007) 535.
- [33] GARCIA, J. et al., Nuclear Fusion **55** (2015) 053007.
- [34] MAGGI, C. F. et al., Nuclear Fusion **55** (2015) 113031.
- [35] KING, D., Tritium Neutral Beam Injection on JET: Calibration and Plasma Measurements, in *this special issue*, 2023.
- [36] PANKIN, A. et al., Computer Physics Communications **159** (2004) 157.
- [37] BRESLAU, J. et al., TRANSP, [Computer Software] \url{https://doi.org/10.11578/dc.20180627.4}, 2018.
- [38] CARVALHO, I. S. et al., Fusion Engineering and Design **124** (2017) 841.
- [39] HOBIRK, J., The JET hybrid scenario in D, T and DT, in *this special issue*, 2023.
- [40] ANGIONI, C., Plasma Physics and Controlled Fusion **63** (2021) 73001.
- [41] LOMANOWSKI, B. et al., Nuclear Fusion **62** (2022) 66030.
- [42] SCHNEIDER, P. A. et al., Nuclear Fusion **53** (2013) 073039.
- [43] FRASSINETTI, L. et al., Review of Scientific Instruments **83** (2012) 13506.
- [44] HAWKES, N. C. et al., Review of Scientific Instruments **89** (2018) 10D113.
- [45] GROEBNER, R. J. et al., Physics of Plasmas **5** (1998) 1800.
- [46] SCHNEIDER, P. A. et al., Plasma Physics and Controlled Fusion **54** (2012) 105009.
- [47] LECHTE, C. et al., Plasma Physics and Controlled Fusion **59** (2017) 75006.
- [48] MENESES, L. et al., Fusion Engineering and Design **86** (2011) 552.

- [49] Conway G D et al., Doppler reflectometry on ASDEX Upgrade: Foundations and latest results, in *8th International Reflectometry Workshop - IRW8 (St.Petersburg) 2-4th May 2007*, volume 8, pages 2-4, 2007.
- [50] RYTER, F. et al., Plasma Physics and Controlled Fusion **48** (2006) B453.
- [51] PEREVERZEV, G. V. et al., IPP Report **5/98** (2002).
- [52] DUNNE, M. G. et al., Plasma Physics and Controlled Fusion **59** (2017) 25010.
- [53] LUDA, T. et al., Nuclear Fusion **60** (2020) 036023.
- [54] SUTTROP, W. et al., Plasma Physics and Controlled Fusion **39** (1997) 2051.
- [55] PETTY, C. C. et al., Phys. Rev. Lett. **74** (1995) 1763.
- [56] ANGIONI, C. et al., Physics of Plasmas **25** (2018) 82517.
- [57] PINZÓN, J. R. et al., Plasma Physics and Controlled Fusion **59** (2017) 35005.
- [58] WILSON, H. R. et al., Physics of Plasmas **9** (2002) 1277.
- [59] VIEZZER, E. et al., Nuclear Fusion **58** (2018) 026031.
- [60] FRASSINETTI, L., Effect of the isotope mass on pedestal structure, transport and stability in D, DT and T plasmas at constant beta<sub>N</sub> and gas rate in JET-ILW, in *this special issue*, 2023.
- [61] FRASSINETTI, L. et al., Nuclear Fusion **61** (2021) 126054.
- [62] KALLENBACH, A. et al., Nuclear Fusion **49** (2009) 045007.
- [63] SCHNEIDER, P. A. et al., Plasma Physics and Controlled Fusion **63** (2021) 64006.
- [64] MAHDAVI, M. A. et al., Physics of Plasmas **10** (2003) 3984.
- [65] HUBBARD, A. E., Plasma Physics and Controlled Fusion **42** (2000) A15.
- [66] URANO, H. et al., Nuclear Fusion **48** (2008) 045008.
- [67] GROEBNER, R. J. et al., Nuclear Fusion **49** (2009) 085037.
- [68] LEYLAND, M. J. et al., Nuclear Fusion **53** (2013) 083028.
- [69] Surface interaction database EIRENE, <http://www.eirene.de/html/tritium.html>.
- [70] MAKAROV, S. O. et al., Nuclear Fusion **63** (2023) 26014.
- [71] NYSTRÖM, H. et al., Nuclear Fusion **62** (2022) 126045.
- [72] BIRKENMEIER, G. et al., Nuclear Fusion **62** (2022) 86005.
- [73] PLANK, U. et al., Plasma Physics and Controlled Fusion **65** (2022) 14001.
- [74] SOLANO, E., Isotope dependence of L-H power threshold in JET-ILW, in *this special issue*, 2023.
- [75] FABLE, E. et al., Plasma Physics and Controlled Fusion **55** (2013) 124028.
- [76] TARDINI, G. et al., Nuclear Fusion **61** (2021) 036030.
- [77] CHALLIS, C. D. et al., Nuclear Fusion **29** (1989) 563.
- [78] ERIKSSON, L.-G. et al., Nuclear Fusion **33** (1993) 1037.
- [79] GÖRLER, T. et al., Journal of Computational Physics **230** (2011) 7053.
- [80] FRIEMAN, E. A. et al., The Physics of Fluids **25** (1982) 502.
- [81] BRIZARD, A. J. et al., Rev. Mod. Phys. **79** (2007) 421.
- [82] KIM, H.-T., Validation of DT fusion power prediction capability against 2021 JET DT experiments, in *this special issue*, 2023.
- [83] ROMANELLI, M. et al., Nuclear Fusion **55** (2015) 93008.
- [84] MORDIJCK, S., Nuclear Fusion **60** (2020) 82006.
- [85] MASLOV, M., JET DT scenario with optimized non thermal fusion, in *this special issue*, 2023.